Available online at www.sciencedirect.com

SciVerse ScienceDirect

Geochimica et Cosmochimica Acta 78 (2012) 28–50

Geochimica et Cosmochimica Acta

www.elsevier.com/locate/gca

Enrichment of Rh, Ru, Ir and Os in Cr spinels from oxidized magmas: Evidence from the Ambae volcano, Vanuatu

Jung-Woo Park *, Ian H. Campbell, Stephen M. Eggins

Research School of Earth Sciences, Australian National University, Canberra 0200, ACT, Australia

Received 12 April 2011; accepted in revised form 2 November 2011

Abstract

Experimental studies, performed under oxidized conditions ($fO_2 > QFM + 2$, where QFM is quartz–fayalite–magnetite oxygen buffer), have shown that Rh, Ru, Ir and Os are strongly compatible with Cr spinel, whereas empirical studies of Cr spinels from ultramafic–mafic rocks suggest that the experimental results may overestimate the partition coefficients. We report laser-ablation inductively coupled plasma mass spectrometry (LA-ICP-MS) analyses of platinum-group elements (PGE), Au and Re abundances in Cr spinels from the Ambae volcano, Vanuatu ($fO_2 = QFM + 2.5$), the Jimberlana layered intrusion, western Australia, and the Bushveld complex, South Africa ($fO_2 \sim QFM$). The results show that Rh and IPGEs (Iridium-group PGE; Ru, Ir, Os) partition strongly into the Cr spinels that crystallized from the oxidized Ambae lavas whereas most of the Cr spinels from the more reduced Jimberlana layered intrusion and the Bushveld complex contain no detectable PGE, Au or Re, with exception of ~10 ppb of Ir in some Jimberlana Cr spinels. In the Ambae Cr spinels, Rh, Ru and, to lesser extent Os, are positively correlated with Fe^{3+}, Ni and V. The homogeneous distribution of Rh and IPGEs in LA-ICP-MS time-resolved spectra indicates that these elements are in solid solution in Cr spinels. Pt–Fe alloys occur as inclusions within the Ambae Cr spinels, which indicate that the Ambae melt was saturated with Pt.

Our results show that partitioning of Rh, Ru and Ir into Cr spinels increases with increasing oxygen fugacity, which suggests that the high concentrations of these elements in the Ambae Cr spinels are due to the high oxygen fugacity of the host magma. Therefore, Cr spinels may play an important role in controlling the concentrations of Rh and IPGEs during fractional crystallization of oxidized ultramafic–mafic magmas and during partial melting of oxidized arc mantle.

1. INTRODUCTION

Cr spinel is considered to be an important host for platinum-group elements (PGEs). The correlation between whole rock Cr and PGE contents observed in various magmatic suites (Hamlyn et al., 1985; Crocket and Macrae, 1986; Brugmann et al., 1987), and the enrichment of PGEs in chromitites from the layered intrusions, ophiolites and alpine-type peridotites (Peck et al., 1992; Zhou et al., 1998; Ahmed and Arai, 2002; Buchl et al., 2004; Ahmed et al., 2009), suggest a genetic link between PGE concentrations and Cr spinels. Whether the observed trends are controlled mainly by PGEs in solid solution in the Cr spinels or platinum group minerals (PGMs) and PGE-bearing sulfides that are entrapped in Cr spinels during their crystal growth remains unresolved.

Experimental studies on partitioning of PGEs between spinels and silicate melts (Capobianco and Drake, 1990; Capobianco et al., 1994; Righter et al., 2004) showed that significant amounts of Rh and IPGEs (Iridium-group PGE; Ru, Ir, Os) can be held in solid solution in spinel species including Cr spinels, with high partition coefficients for Ir ($D_{Ir} = 5$–22,000), Ru ($D_{Ru} = 20$–4000) and Rh ($D_{Rh} = 41$–530), under oxidized conditions ($fO_2 > QFM + 2$, where QFM is quartz–fayalite–magnetite oxygen buffer). However, Cr spinels often occur in association with PGMs and PGE-bearing sulfide inclusions in natural samples from layered intrusions, ophiolites and komatiitic basalts, and mass balance constraints

* Corresponding author. Tel.: +61 2 612 57615.
E-mail address: jung.park@anu.edu.au (J.-W. Park).

0016-7037/$ - see front matter © 2011 Elsevier Ltd. All rights reserved.
doi:10.1016/j.gca.2011.11.018

indicated that the main hosts for the PGEs in these rocks are PGM and sulfide. In situ analysis of PGEs in Cr spinels from the Merensky Reef, the Bushveld complex (Ballhaus and Sylvester, 2000) and komatiitic basalts, ferropicritic basalts and tholeiitic basalt from the Abitibi Greenstone Belt (Fiorentini et al., 2004) further revealed that most of the Cr spinel grains contain PGMs and that the concentrations of PGEs in solid solution are below the detection levels (tens of ppb) of the method used. Pagé et al. (2011) analyzed Cr spinels from podiform- and stratiform chromitites and lavas from different tectonic settings and reported that all PGEs were below detection limits, except for Cr spinels from komatiites which contain Ru (~450 ppb), Os (~19 ppb) and Ir (~20 ppb). The discrepancy between experimental studies and natural observations may mean that the experimental studies have overestimated the partition coefficients for PGEs between silicate melts and Cr spinels (Pagé et al., 2011). However, it should be noted that all the analyzed samples of the previous LA-ICP-MS studies were from relatively reduced magmatic environments ($fO_2 \leqslant$ QFM) and there is no reported study of PGE abundances in Cr spinels that formed under oxidized condition similar to those of the experimental studies ($fO_2 >$ QFM + 2).

We have made in situ LA-ICP-MS analyses of PGEs, Au and Re in Cr spinels from the oxidized lavas of the Ambae volcano, Vanuatu, south-western Pacific, the relatively reduced Jimberlana layered intrusion, western Australia and the Bushveld complex, South Africa. Our results confirm the compatibility of Rh and IPGEs in Cr spinels that crystallize under oxidized conditions and permit evaluation of the influence of factors such as cooling rate and oxygen fugacity on the partitioning of Rh and IPGE into Cr spinel. We also measured whole rock PGE contents of the Ambae lavas to calculate empirical partition coefficients for Rh, Ru and Ir between Cr spinel and melt.

2. BACKGROUND AND SAMPLES

2.1. Ambae volcano

Ambae is an active volcano in the Vanuatu island arc, located in a segment affected by collision with the D'Entrecasteaux zone, an Eocene-Oligocene island arc complex on the subducting Australian-India plate (Collot et al., 1985). The detailed geological features of the Ambae volcano, including the relationship between rock types and the sequence of volcanism, are described in Warden (1970), and the petrology and geochemistry in Gorton (1977) and Eggins (1993). The Ambae lavas are subaerial high-K calc-alkaline basalts that range in composition from high alumina basalts (4.5 wt.% MgO) to picritic basalts (~23 wt.% MgO) (Eggins, 1993). The lavas have been divided into the two groups: an older high-Ti suite (HTS) and a younger low-Ti suite (LTS), based on mineralogy, geochemistry and stratigraphy (Eggins, 1993). The oxygen fugacity (fO_2) calculated from the olivine–spinel geobarometer of Ballhaus et al. (1991) is QFM + 2.5 (Eggins, 1993).

The samples used in this study are mafic LTS lavas in which the compositional variation is controlled by the accumulation and distribution of early-crystallized olivine, clinopyroxene and Cr spinel phenocrysts. The analyzed Cr spinels were from samples with a wide variation of MgO contents (10.8–23.4 wt.%). Cr spinels occur as small (<200 μm) euhedral micro phenocrysts in matrix, similar-sized euhedral to subhedral inclusions in olivine phenocrysts, and rarely in clinopyroxene.

2.2. Jimberlana layered intrusion and Bushveld complex

The Jimberlana layered rocks are subdivided into three series: the upper layered series, the lower layered series, and the marginal layered series (see Fig. 1 Roeder and Campbell, 1985). The Jimberlana Cr spinels analyzed in this study are from an olivine cumulative layer near the bottom of the lower layered series. Rocks in this layer are thought to have crystallized from a primitive magma and contain low Cu (20–50 ppm), which is interpreted to indicate the absence of cumulate sulfide competing for the PGEs during crystallization of the Cr spinels (Keays and Campbell, 1981).

Maier et al. (1996), Mondal and Mathez (2007) and Naldrett et al. (2009) have described the Bushveld chromitites. The Cr spinels used in this study are from the chromitite layers of the UG2 reef and the Merensky reef, as exposed at the Karee and Impala mines, respectively. Both the UG2 Reef and the Merensky Reef are a PGE-rich, sulfide-bearing cumulate layer (0.1% modal sulfide for the UG2 and 0.2–0.7% modal sulfide for the Merensky; Maier et al., 1996) in the upper critical zone of the Bushveld complex, suggesting that sulfide liquids and Cr spinels were in equilibrium during formation of chromitite layers (Mondal and Mathez, 2007).

3. ANALYTICAL TECHNIQUES

3.1. Cr spinel analysis

Cr spinel concentrates were obtained from the Ambae lavas by conventional heavy liquid and electromagnetic separation techniques. The Cr spinels were then handpicked, mounted in epoxy, and polished. Polished thin sections were also prepared for the Ambae lavas for modal analysis and additional Cr spinel analysis. Analyses of the Cr spinels from the Jimberlana layered intrusion (Keays and Campbell, 1981) and the Bushveld complex were carried out on polished thin sections and epoxy mounts, respectively.

Major element compositions and the Cr contents for the Cr spinels, olivines, clinopyroxenes and Ti–Fe oxides were obtained using the CAMECA SX100 electron microprobe at the Research School of Earth Sciences (RSES), the Australian National University (ANU). The beam conditions for Cr spinel analysis were 15 kV and 40 nA, focused to 1 μm, and for silicates and Ti–Fe oxides analysis were 15 kV and 20 nA. The FeO and Fe_2O_3 contents of Cr spinels were calculated from charge balance and stoichiometry, after subtracting the ulvöspinel component based on the TiO_2 content in the spinel (e.g. Murck and Campbell, 1986). Cr spinels were first analyzed by CAMECA SX100 or JEOL6400 scanning electron microscopy at the ANU to select locations for detailed analyses. Pt–Fe alloys were

semi-quantitatively analyzed with the JEOL6400 using pure PGE metal standards. The concentrations of PGEs, Au, Re and other trace elements (V, Mn, Co, Ni, Cu and Zn) in the Cr spinels were then determined by LA-ICP-MS at the RSES, at the ANU. This system consists of a Lambda Physik Complex 110 excimer laser ($\lambda = 193$ nm) and ANU-designed HelEx ablation cell, coupled to an Agilent 7500 ICP-MS, with He as the carrier gas. For the additional analyses of Cr spinels from the Ambae lavas, the Jimberlana layered intrusion and the Bushveld complex we used an Agilent 7700 ICP-MS with the same laser ablation system and data reduction procedure.

LA-ICP-MS analyses were performed using a laser pulse rate of 10 Hz and spot sizes that varied between 81 and 178 μm. Each analysis consisted of 35 s of background measurement followed by 45 s of sample ablation. A NIST 612 glass standard was used as the external standard for V, Mn, Ni, Zn and Co with Ti obtained from electron microprobe analysis employed as the internal standard. CANMET po727 FeS standard, described in Fonseca et al. (2009) and Barnes et al. (2008), containing ~40 ppm of all PGE, was employed for calibration of Pd, Pt, Rh, Ru, Ir, Os and Au. Co concentrations, measured by LA-ICP-MS against NIST 612, were used as the internal standard to correct for yield differences in the PGEs, Au and Re between samples and the standard. Standards were analyzed before and after analyses of 5–8 unknown points. Data reduction was performed following the method of Longerich et al. (1996). The detection limits for the analyzed elements were calculated using the relationship described in Longerich et al. (1996) and Sylvester and Eggins (1997). In order to check the homogeneity of CANMET po727 FeS standard and the stability of the ICP-MS, the CANMET po727 FeS standard was analyzed as an unknown sample. The standard deviations for the analyses of the CANMET po727 FeS standard of all PGEs were <2% (Table 1). An in-house PGE glass standard and a NIST 612 standard were analyzed using the CANMET po727 FeS standard to assess the data precision and accuracy of the analyses of PGEs and Re. The PGE contents in the in-house PGE silicate glass standard of nominal anorthite-diopside eutectic composition were independently measured by Guilherme Mallmann at the ANU using electron microprobe and LA-ICP-MS. Our analyses of standards agree with the values reported in the literature and with the values independently measured by Guilherme Mallmann, as reported in Table 1.

The isotopes used to determine trace elements and PGE concentrations in this study were as follows: ^{47}Ti, ^{51}V, ^{55}Mn, ^{59}Co, ^{62}Ni, ^{66}Zn, ^{101}Ru, ^{103}Rh, ^{105}Pd, ^{192}Os, ^{193}Ir and ^{195}Pt. In terms of PGEs, these isotopes were chosen in order to maximize signal to noise ratios and minimize isobaric interferences. The isobaric interferences produced by metal oxides (MO^+) and metal argides (MAr^+) were determined from tests conducted on synthetic Ni–sulfide and pure Cu metal (C-430, Fisher Scientific Company), which have very low PGE abundances, with the assumption that the blank-corrected signals of ^{101}Ru, ^{103}Rh and ^{105}Pd in Ni–sulfide and Cu metal are produced only by argide interferences. The production rates of $^{61}Ni^{40}Ar^+$, $^{63}Cu^{40}Ar^+$ and $^{65}Cu^{40}Ar^+$, which interfere with ^{101}Ru, ^{103}Rh and ^{105}Pd, respectively, were small and found to fall within the range $MAr^+/M^+ = 2.2–2.4 \times 10^{-4}$. Isobaric interferences were subtracted from the time-integrated signal, based on the measured Cu and Ni count rates in the Cr spinels and the argide production rates. Because of its higher isotopic abundance (41%) ^{192}Os was chosen for Os determination although ^{192}Os has interference from ^{192}Pt in both sample and standard. The isobaric interference by ^{192}Pt at ^{192}Os was negligible in samples because the Pt concentration in the analyzed Cr spinels was below detection. ^{192}Os interferes with ^{192}Pt in the sulfide standard, which is corrected using count rates of ^{195}Pt and relative abundance of ^{192}Pt. The interference corrections on ^{101}Ru, ^{103}Rh and ^{192}Os in Cr spinels were 2–7%, 0.5–3.5% and 0.4–0.5%, respectively. Data were acquired in the time resolved mode

Table 1
Estimates of precision and accuracy of the LA-ICP-MS concentration measurements (ppm).

Reference material	Laboratory	Method	n	Ru	Rh	Pd	Os	Ir	Pt	Re
po727[a]	CANMET	LA-ICP-MS	43 avg.	36.5	41.6	43.4	46.7	48.0	35.5	
			1σ	0.3	0.3	0.3	2.6	1.2	0.5	
po727	This study	LA-ICP-MS	6 avg.	36.3	41.7	43.3	47.3	48.5	35.7	
			1σ	0.3	0.7	1.9	0.5	0.8	1.3	
PGE glass	ANU	LA-ICP-MS	5 avg.	2415[b]	160[c]	80[c]	231[b]	511[b]	5044[c]	2218[c]
			1σ	20	4	2	1	5	62	39
		EPMA	15 avg.	2340	266				5166	2290
			1σ	111	89				332	64
PGE glass	This study	LA-ICP-MS	7 avg.	2362	198	66	239	546	5289	2395[c]
			1σ	69	8	2	10	13	193	45
NIST612[d]			4 avg.		0.90	1.09			2.59	
			1σ		0.01	0.09			0.03	
NIST612	This study	LA-ICP-MS	6 avg.		0.92	0.75			2.24	
			1σ		0.06	0.05			0.40	

[a] Data from Barnes et al. (2008).
[b] Data were calibrated against CANMET po727.
[c] Data were calibrated against NIST 612.
[d] Data from Sylvester and Eggins (1997).

to monitor the presence of heterogeneity in the Cr spinels (e.g. PGM inclusion). Micro inclusions were identified from abrupt intensity spikes during the analysis, which were excluded from the trace element and PGE concentration calculations.

3.2. Whole rock analysis

Major elements in four whole rock samples were analyzed by XRF Phillips PW2400 spectrometer at the RSES, the ANU. XRF fusion discs were made using about 0.27 g sample powder and 1.72 g of lithium borate eutectic flux ($Li_2B_4O_7$:$LiBO_2$ mass ratio = 12.22). Trace element concentrations were determined by LA-ICP-MS analyses of the recycled whole rock XRF disks, using the same LA-ICP-MS system used in Cr spinel analysis. Analyses were obtained at a laser repetition rate of 7 Hz with a spot size of 137 μm. Each spot analysis consisted of 25 s of background measurement followed by 65 s of sample ablation. The NIST 612 standard was analyzed before and after analyses of four points on each sample. The BCR-2g (Gao et al., 2002) was used to monitor quality control. Ca concentrations measured by XRF were used as an internal standard to determine the absolute concentration of elements. Analytical uncertainties were ±1–5% (2σ), depending on the elements.

Whole rock PGE and Re concentrations of the Ambae lava samples were measured using a Ni–sulfide fire assay – isotope dilution method, which was modified from Ravizza and Pyle (1997) and Setiabudi et al. (2007). Five grams of a powdered sample, 0.5 g of Ni, 0.25 g of S, 5 g of sodium borax were weighed to five decimal places. These were mixed thoroughly on clean papers and transferred into porcelain Coors™ crucibles. A mixed spike solution of PGEs (^{99}Ru, ^{105}Pd, ^{185}Re, ^{191}Ir, and ^{195}Pt) was added into the sample powder and weighed. A second outside crucible, containing ~0.1 g of flour was used to provide reducing conditions at the beginning of the fusion. The crucibles were dried in the furnace for 60 min at 100 °C to remove absorbed water from the sample. The mixture was then fused in a preheated furnace at 1100 °C for 30 min and quenched by removing the crucible from the furnace. N_2 gas was introduced into the open furnace with the flow rate of ~0.03 m^3/min to provide reducing conditions during fusion. After quenching, the crucible was broken open, the NiS beads were collected and dissolved in 150 ml of 6 N HCl. The solutions were then filtered through a Millipore filter paper and washed with Milli-Q water, prior to digestion of the filter paper in 4 ml aqua regia (1 ml of 14 N HNO_3 and 3 ml of 8 N HCl). After complete digestion, the solutions were dried down to ~100 μl, then diluted with 5 ml of 2% HNO_3 and refluxed at 100 °C for 2 h. This final solution was allowed to cool, stored overnight, and centrifuged shortly before measurement by ICP-MS.

A single collector ICP-MS (Agilent 7500) at the ANU was used to measure the isotopes of PGEs and Re. The sensitivities in each analysis were 4.6–5.8 × 10^4 cps/ppb for mass 89, 2.0–2.8 × 10^4 cps/ppb for mass 140 and 1.8–2.2 × 10^4 cps/ppb for mass 205. The reproducibility of individual analyses using ~0.5–1 ppb in-house PGE standard were between 0.2–1.1% for ^{99}Ru/^{101}Ru, 0.6–1.8% for ^{105}Pd/^{108}Pd, 0.1–0.6% for ^{185}Re/^{187}Re, 0.2–0.5% for ^{191}Ir/^{193}Ir and 0.5–0.6% for ^{195}Pt/^{194}Pt ($2\sigma_{aver}$). Molecular isobaric interferences on the analyzed isotopes were monitored by measuring interference solutions of Ni, Cu, Zn, Co, Hf, Mo, Zr and Ta. The effects of the molecular interference were subtracted using measured oxide and argide production rates. The corrections are <0.5% for Ir, Rh, Pd, Pt and Re. The corrections for Ru vary from 16% to 45% except for an analysis of sample 70531 (~80%) and two analyses of sample 68638 (~60%).

Concentrations of Pd, Pt, Ru, Ir and Re were determined by isotope dilution. Concentrations of monoisotopic Rh were corrected by the method employed by Meisel et al. (2003) using count rates of ^{103}Rh and ^{106}Pd, with assumption that any loss of Rh during the analytical procedure was similar to loss of Pd. The number of atoms of ^{103}Rh in the sample + spike mixture N^{103Rh}_{mix} is calculated as follows:

$$N^{103Rh}_{mix} = \frac{N^{106Pd}_{mix} \times C^{103Rh}_{mix}}{C^{106Pd}_{mix}} \times \frac{C^{103Rh}_{standard}}{C^{106Pd}_{standard}} \times \frac{N^{103Rh}_{standard}}{N^{106Pd}_{standard}}$$

where N^{A}_{mix} and $N^{A}_{standard}$ are the number of atoms of the isotope A in the sample + spike mixture and standard, respectively. C^{A}_{mix} and $C^{A}_{standard}$ are the count rates of the isotope A in the sample + spike mixture and standard, respectively.

Table 2
Procedural blanks and PGE analyses of TDB-1 (ppb).

	Re	Pd	Pt	Rh	Ru	Ir
Procedural blank ($n = 4$)	0.008	0.010	0.005	0.0005	0.0011	0.0004
Limit of detection (3σ)	0.002	0.006	0.005	0.0007	0.0010	0.0004
TDB-1 (CANMET)						
This study	0.75	20.7	4.26	0.360	0.158	0.058
This study	0.63	19.7	4.07	0.340	0.149	0.054
This study	0.63	20.5	4.50	0.365	0.142	0.063
This study	0.71	26.7	4.02	0.426	0.167	0.056
Average ($n = 4$)	0.68 ± 0.10	21.9 ± 5.4	4.21 ± 0.28	0.373 ± 0.064	0.154 ± 0.018	0.058 ± 0.006
M&M[a] ($n = 7$)	0.79 ± 0.04	24.3 ± 3.4	5.01 ± 0.34	0.471 ± 0.078	0.198 ± 0.016	0.075 ± 0.018
P[b] ($n = 8$)		24.8 ± 1.4	4.40 ± 0.30			0.078 ± 0.006

Errors are quoted at 2σ.
[a] Meisel and Moser (2004), high pressure asher (HPA) digestion isotope dilution-ICP-MS.
[b] Peucker-Ehrenbrink et al. (2003), Ni–sulfide fire assay-isotope dilution.

Table 3
Selected analytical results of major, trace and platinum group elements data for the Ambae lavas.

Sample	MgO	Ti	Mn	Zn	Ni	Cr	Co	Re	Pd	Pt	Rh	Ru	Ir	$(Pd/Ir)_N$	*n*
Aphyric lava															
68638	10.7	4605	1194	54	146	500	42	0.283	3.07	4.60	0.154	*0.05*	0.050	53	2
								11	*1*	*8*	*12*	*22*	*40*		
Olivine-clinopyroxene-chromite cumulate lavas															
70531	15.4	3983	1211	50	250	791	54	0.126	2.88	5.88	0.218	0.068	0.143	17	3
								5	*6*	*15*	*3*	*8*	*14*		
70566	17.5	3774	1184	48	334	1124	58	0.150	1.65	3.05	0.164	0.086	0.115	12	2
								0.2	*1*	*3*	*8*	*7*	*13*		
70492	23.4	2975	1212	50	506	1531	73	0.185	4.12	7.48	0.267	0.178	0.276	13	2
								0.2	*0.1*	*6*	*6*	*5*	*17*		

MgO in wt.%, Ti, Mn, Zn, Ni, Cr and Co in ppm, PGE and Re in ppb; PGE and Re concentrations are average of several replicate analyses and the number of replicates are denoted by *n*; Reproducibility (in italics) is expressed as % SD of the average; Note that Ru concentration in sample 68638 with high NiAr interference correction (~60%) is presented in italic with two decimal places.

Procedural blanks were determined from sample-free analyses using 10 g of sodium borax, 0.5 g of Ni and 0.25 g of S for every session. Accuracy and precision were tested by replicate analysis of the international standard TDB-1 (CANMET diabase). Procedural blanks for the method, limits of detection (3σ) and PGE analyses of TDB-1 are reported in Table 2. Procedural blanks were subtracted from the data. The blank corrections were <2% for all PGEs expect Re for which it was 3–6%. Reproducibility of TDB-1 analyses is <15% and the results agree with values reported by Meisel and Moser (2004) and Peucker-Ehrenbrink et al. (2003) within error (2σ).

4. RESULTS

4.1. Whole rock abundances of PGE and Re

The selected major, trace, platinum-group elements abundances in an aphyric and three phenocryst-rich Ambae lavas are presented in Table 3 and the PGE and Re concentrations in the samples are shown as chondrite-normalized abundances in Fig. 1. All the Ambae samples are characterized by fractionated patterns with negative Ru anomalies, which are also found in some picrites from the Lesser Antilles arc (Woodland et al., 2002). The aphyric lava (sample 68638) shows a more fractionated pattern ($(Pd/Ir)_N = 53$) compared with the samples that contain abundant phenocrysts ($(Pd/Ir)_N = 12–17$). This suggests that the accumulated phenocryst assemblage is enriched in Ir relative to Pd (Fig. 1a). The chondrite-normalized PGE pattern and absolute abundance of the aphyric lava is similar to the arc picrites from Grenada, Lesser Antilles arc (Fig. 1b). Also plotted in Fig. 1b for comparison are the estimated PGE concentrations in high Mg basalts and tholeiitic basalts that are considered to be parental magmas of the Bushveld complex (Barnes and Maier, 2002). The PGE concentrations in the Ambae aphyric lava are at least five times lower than they are in the high Mg basalts and tholeiitic basalts (Fig. 1b). The PGE contents of the Jimberlana magma are not particularly low compared to other volacanic–ultramafic association (Keays and Campbell, 1981).

4.2. Homogeneity of PGE in Cr spinels

Many studies have found PGE-bearing inclusions, such

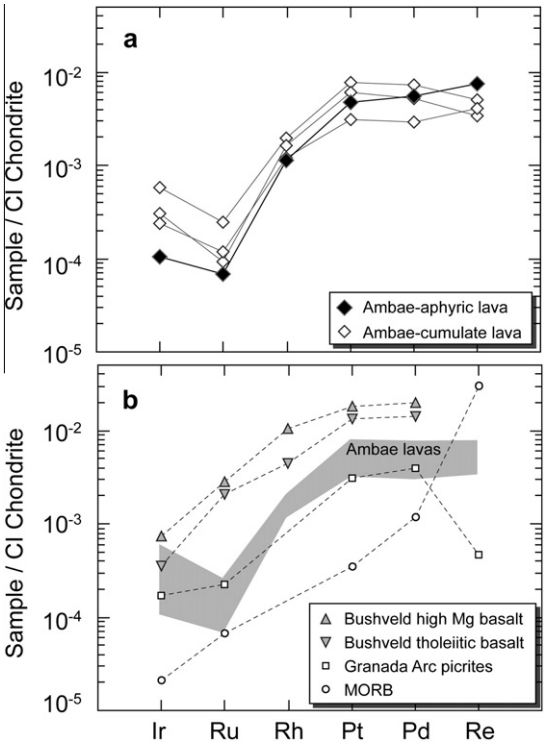

Fig. 1. (a) CI chondrite-normalized PGE and Re patterns for the Ambae lavas. (b) The Ambae lavas (gray field) are compared with average of arc picrites ($n = 8$,>13 wt.% MgO) from the Grenada, Lesser Antilles arc (Woodland et al., 2002), estimates of a high Mg basalt and a tholeiitic basalt from the Bushveld complex (Barnes and Maier, 2002), and the mean MORB (Dale et al., 2009 and references therein). Chondrite values from Anders and Grevesse (1989).

as alloys and clusters, in Cr spinels with sizes that vary from sub-micron to micron scale (Ballhaus and sylvester, 2000; Fiorentini et al., 2004; Locmelis et al., 2011; Pagé et al., 2011). Therefore, it is important to determine whether the PGE abundances in Cr spinel is free of contamination by nuggets of PGE-bearing phases. The presence of such inclusions can be detected in the time-resolved spectra of LA-ICP-MS analyses, if the instrument used has a rapid response time. Under the operating conditions used in this study the ANU HelEx cell has a signal response time of 2 s, which we define as the time taken for the signal to decay by an order of magnitude. As a result any tiny sub-micron PGE-rich phase intersected during analyses is recorded as spikes in signal intensity that rapidly decay back to pre-spike levels.

The Ambae Cr spinels show homogeneous distributions of Rh, Ru, Ir and Os in time-resolved ICP-MS spectra as indicated by the uniform count rates of these elements during the ablation (Fig. 2). At lower concentrations, the variation in the time resolved count rates of Ru, Ir and Os becomes higher because of lower analytical precision resulting from low signal intensity. This phenomenon has been also observed in LA-ICP-MS analyses on experimental products such as synthetic glasses and silicates (Ertel et al., 2001; Brenan et al., 2003, 2005). The observations from the LA-ICP-MS time-resolved spectra indicate that PGEs are homogeneous at the spatial resolution of the analyses, and are therefore likely to be in solid solution in Cr spinels. Furthermore, Rh, Ru and Os contents in Cr spinels show correlations with Cr spinel compositional parameters such as Fe^{3+}/R^{3+} ($Fe^{3+}/R^{3+} = Fe^{3+}/(Cr + Al + Fe^{3+})$), which suggest that their concentrations were controlled by crystallochemical mechanism and not by inclusions.

4.3. Metal micro-inclusions in the Ambae Cr spinels

During this study more than 150 Cr spinels and 70 olivines from the Ambae lavas were imaged by scanning electron microscopy (SEM) and three Cr spinels were observed to contain PGM inclusions. The size of these inclusions was ~10 μm. Eighty-seven Cr spinels were analyzed by LA-ICP-MS and five Cr spinels show nine PGE spikes in time resolved spectra, which we attribute to micro-inclusions (Fig. 3). The occurrence of PGE-bearing inclusions in the Ambae Cr spinel is far less common than reported by previous LA-ICP-MS studies for Cr spinels from the Merensky

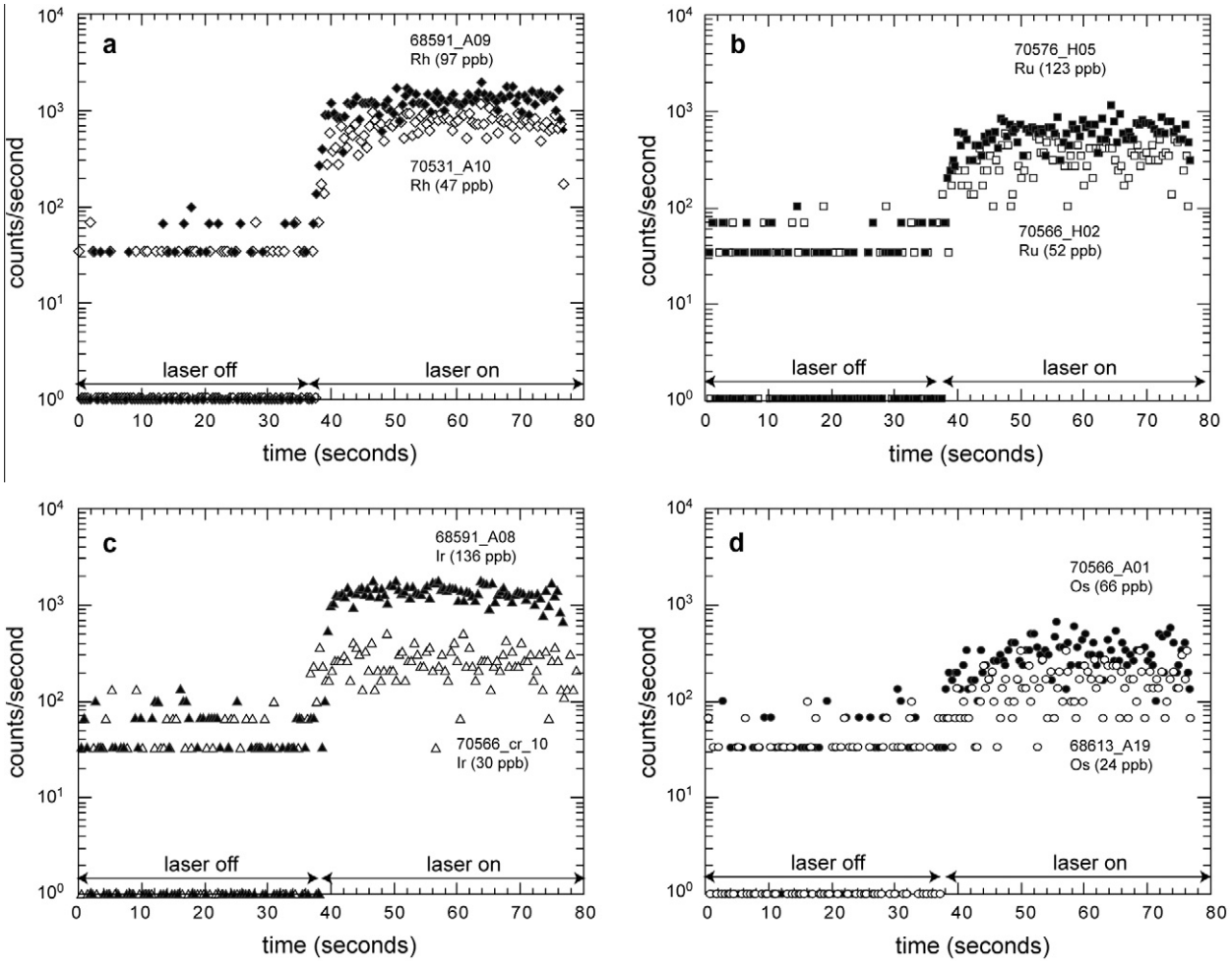

Fig. 2. Time-resolved LA-ICP-MS spectra of (a) Rh, (b) Ru, (c) Ir and (d) Os in Cr spinels from the Ambae lavas. Variability is higher at lower concentrations due to low signal intensity.

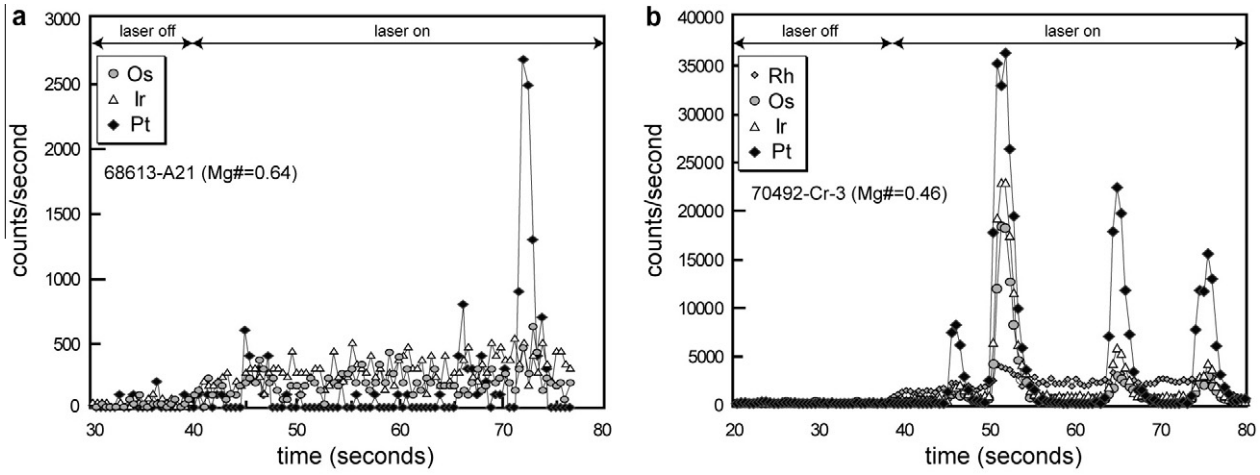

Fig. 3. Time-resolved LA-ICP-MS spectra for Cr spinels with PGE-bearing inclusions from the Ambae lavas. Co-incident spikes of Pt, Ir and Os, and to a lesser extent Rh are interpreted to be Ir–Os–(Rh)-bearing Pt–Fe alloys, as also observed by SEM. (a) Pt–Fe alloys from high Mg# Cr spinel (Mg# = 0.64) are characterized by very low Ir, Os and Rh signals. (b) Pt–Fe alloys from low Mg# Cr spinel (Mg# = 0.46). The abundances of Ir and Os vary from grain to grain but are generally higher in Pt–Fe alloys from low Mg# Cr spinels than in those from high Mg# Cr spinels.

Table 4
Electron microprobe data of Pt–Fe-alloys from the Ambae lavas (wt.%).

Cr spinel host		Alloy							
Sample	Spinel Mg#	Fe	Pt	Rh	Os	Ir	Total	(Ir + Os)/Pt	Rh/Pt
68591-H01	54.8	5.3	89.0	0.81	1.6	3.0	99.8	0.052	0.009
	54.8	4.9	81.1	0.90	7.7	5.4	100.0	0.161	0.011

reef, Bushveld complex (Ballhaus and Sylvester, 2000) and from komatiitic basalts, ferropicritic basalts and tholeiitic basalt from the Abitibi Greenstone Belt (Fiorentini et al., 2004). These studies reported that more than half of the analyzed Cr spinel grains contained such phases.

The most common type of inclusion found in the Ambae Cr spinels is a Pt–Fe alloy which contains minor Ir, Os and Rh. The compositions of two Pt–Fe alloys measured by EPMA are reported in Table 4. The compositions of nine additional Pt–Fe alloys inclusions observed during LA-ICP-MS analysis were determined according to the method of Halter et al. (2002) (Appendix A; Table A1). Some of these Pt–Fe alloys are polymetallic with some containing Rh and rarely Ru. In LA-ICP-MS spectra the signals for Ir and Os are often higher in Pt–Fe alloys from the low Mg# Cr spinels (Mg# < 0.6; Mg# = Mg/(Mg + Fe^{2+})) than in the high Mg# Cr spinels (Mg# > 0.6) (Fig. 3). A plot of (Ir + Os)/Pt values in these alloys against the host spinel Mg#, using the data presented in Tables 4 and A1, shows an increase in (Ir + Os)/Pt with decreasing Mg# of the host Cr spinels (Fig 4a). In contrast, Rh/Pt remains constant as Mg# of the host Cr spinels decreases (Fig 4b).

4.4. Cr spinel chemistry

Major, trace and PGE data for Cr spinels from the Ambae lavas, Jimberlana layered intrusion and Bushveld complex are presented in Tables 5, 6, A3 and A4 and plotted in Figs. 5–9. The compositions of the Ambae Cr spinels are broadly similar to those from island arc high-K calc-alkaline basalts (IACB) (Fig. 5a and b). The Ambae spinels can be distinguished from mid-ocean ridge basalts (MORB) by their low Al_2O_3 contents (Fig. 5c). Mantle Cr spinels were observed in some other arc picritic lavas (e.g. Ramsay et al., 1984). The Ambae Cr spinels are distinguished from Cr spinels in supra subduction zone peridotites ($Fe^{2+}/Fe^{3+} > 2.5$, $TiO_2 < 0.3$ wt.%; Kamenetsky et al., 2001) by their lower Fe^{2+}/Fe^{3+} ratios (<2.5) and higher TiO_2 contents (0.25–1.4 wt.%) (Fig. 5c and d). This indicates that all of the analyzed Ambae Cr spinels are magmatic and not xenocrysts from the mantle. The composition of the Jimberlana and the Bushveld Cr spinels is similar to those reported in previous studies (Roeder and Campbell, 1985; Eales and Reynolds, 1986) showing that the analyzed Cr spinels are representative (Fig. 5). The Cr spinels from the Jimberlana layered intrusion and the Bushveld complex have relatively high Fe^{2+}/Fe^{3+} and low Fe^{3+}/R^{3+} compared to the Ambae Cr spinels at a given Mg# and Al_2O_3, reflecting the lower oxygen fugacity of the Jimberlana and the Bushveld parental magmas (Fig. 5b and d).

Cr spinels from the Ambae lavas contain 14–149 ppb Rh (avg. = 78), 47–162 ppb Ru (avg. = 96), <4–200 ppb Ir (avg. = 44), 11–82 ppb Os (avg. = 40). The concentrations of Pd, Pt, Re and Au were below detection limits of 7 ppb for Pd, 6 ppb for Pt and 3 ppb for Re in all of the Ambae Cr spinels. In contrast, the PGE abundances in Cr spinels from the Jimberlana layered intrusion and the

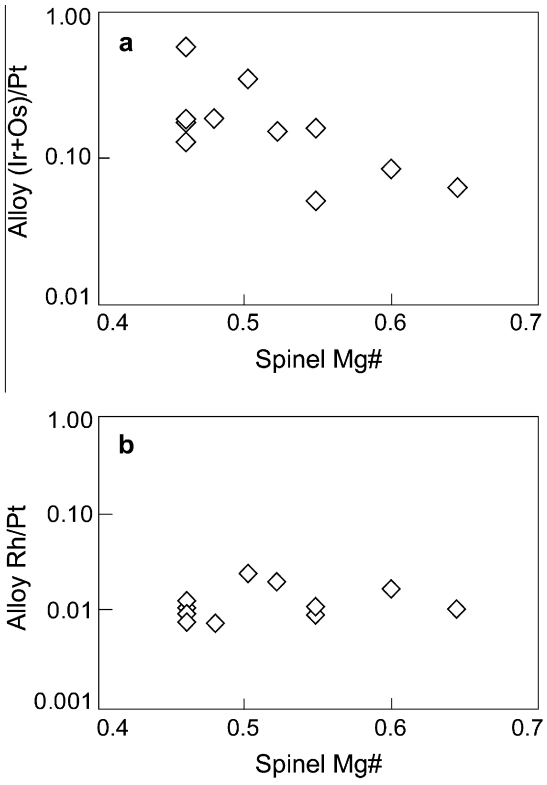

Fig. 4. Variation of (a) (Ir + Os)/Pt and (b) Rh/Pt ratios of Pt–Fe alloys from the Ambae lavas as a function of the host spinel Mg#.

Bushveld complex are below or only slightly above these detection limits, with some grains contain up to ~10 ppb of Ir (Tables 6 and A4). These values are consistent with previous in situ analyses of Cr spinels from the Merensky reef, Bushveld complex in Ballhaus and Sylvester (2000) who reported PGE concentrations of all analyzed Cr spinels to be below detection limits (tens of ppb).

The average PGE concentrations for Cr spinels from each Ambae sample are plotted as CI chondrite-normalized abundances in Fig 6. Cr spinels are enriched in Rh, Ru and Ir relative to the whole rock by at least a factor of a hundred. In spite of the wide variation in the MgO abundances in the analyzed samples (10.5–23.4 wt.%), the PGE patterns of Cr spinels from each sample are within a factor of 2 for Rh, Ru, and Os, whereas Ir varies by nearly an order of magnitude and shows both positive and negative anomalies. Cr spinels with positive or negative Ir anomaly are observed in all Ambae samples except for sample 70576. Sample 70576, which has the lowest MgO contents in this study, only hosts Cr spinels with a negative anomaly (Table A4).

Rhodium and Ru in the Ambae Cr spinels are positively correlated with Fe^{3+}/R^{3+}, whereas the correlation is weak for Os (Fig 7a–c). Rhodium, Ru and Os show positive correlations with each other, reflecting their similar crystal-chemical behavior in Cr spinel (Fig. 8a and b). In contrast, Ir is not correlated with any other PGEs and shows scattered patterns when plotted against spinel composition parameters (Cr#, Mg# and Fe^{3+}/R^{3+}; Cr# = Cr/(Cr + Al)), suggesting that different factors control the Ir concentration in Cr spinel (Figs. 7d and 8c). The trace element Ni and V show positive correlations with Fe^{3+}/R^{3+} and Rh (Figs.7e and f and 8d).

Table 5
Average major element contents of Cr spinels by EPMA.

Location	Ambae	Ambae	Ambae	Ambae	Ambae	Ambae	Jimberlana	Jimberlana	Bushveld	Bushveld
Sample no.	70492	68591	70566	68613	70531	70576	BRD11	NDDI	UG2	Merensky
MgO_{WR}[a]	23.4	17.8	17.5	16.2	15.4	10.5				
n[b]	10	9	17	7	4	8	9	3	10	3
Cr_2O_3 (wt.%)	45.0 (2.5)	46.6 (4.2)	44.7 (6.2)	45.3 (4.1)	46.4 (6.7)	48.7 (1.4)	45.1 (0.7)	39.8 (0.5)	40.9 (1.0)	46.0 (2.4)
Al_2O_3	12.3 (1.2)	10.8 (11)	10.3 (1.7)	11.0 (0.9)	10.0 (0.7)	10.4 (0.6)	15.3 (1.3)	13.8 (0.6)	16.9 (0.5)	14.7 (0.8)
TiO_2	0.67 (0.16)	0.62 (0.15)	0.69 (0.25)	0.58 (0.19)	0.59 (0.30)	0.55 (0.07)	1.2 (0.3)	1.8 (0.3)	1.0 (0.1)	1.2 (0.2)
FeO[c]	18.3 (1.1)	15.8 (1.5)	17.1 (1.2)	18.5 (0.4)	18.7 (0.8)	16.4 (1.7)	19.3 (0.6)	24.5 (0.8)	22.2 (0.4)	21.1 (0.5)
Fe_2O_3 [c]	13.0 (1.9)	13.9 (2.8)	15.7 (3.6)	14.0 (3.0)	13.7 (4.7)	12.6 (0.8)	7.3 (0.5)	12.1 (0.3)	9.7 (0.5)	6.9 (0.7)
MgO	10.4 (0.8)	11.8 (1.1)	10.9 (0.8)	10.0 (0.2)	9.8 (0.5)	11.5 (1.1)	10.2 (0.4)	7.1 (0.4)	8.4 (0.3)	9.1 (0.1)
Total	99.7 (1.1)	99.7 (0.5)	99.5 (0.8)	99.5 (0.6)	99.2 (1.1)	100.1 (0.5)	98.4 (0.8)	99.1 (0.4)	99.1 (0.7)	99.0 (1.5)
Mg#[d]	0.508	0.572	0.532	0.487	0.482	0.555	0.486	0.340	0.404	0.435
Cr# [e]	0.709	0.742	0.741	0.739	0.755	0.758	0.665	0.659	0.618	0.677
Cr^{3+}/R^{3+}, [f]	0.591	0.613	0.595	0.606	0.623	0.638	0.603	0.554	0.542	0.617
Fe^{3+}/R^{3+}, [g]	0.166	0.174	0.200	0.181	0.177	0.158	0.093	0.160	0.123	0.088

[a] MgO_{WR} = MgO content (wt.%) in whole rock.
[b] n = number of separate grains analyzed.
[c] FeO and Fe_2O_3 are obtained by stoichiometric calculations using equations of Murck and Campbell (1986).
[d] Mg# = Mg/(Fe^{2+} + Mg).
[e] Cr# = Cr/(Cr + Al).
[f] Cr^{3+}/R^{3+} = Cr/(Cr + Al + Fe^{3+}).
[g] Fe^{3+}/R^{3+} = Fe^{3+}/(Cr + Al + Fe^{3+}).
Numbers in brackets represent one standard deviation (1σ).

Table 6
Average trace and platinum group element contents of Cr spinels by LA-ICP-MS analysis.

Location	Ambae	Ambae	Ambae	Ambae	Ambae	Ambae	Jimberlana	Jimberlana	Bushveld	Bushveld
Sample no.	70492	68591	70566	68613	70531	70576	BRD11	NDDI	UG2	Merensky
MgO_{WR}[a]	23.4	17.8	17.5	16.2	15.4	10.5				
n[b]	10	9	17	7	4	8	9	3	10	3
V (ppm)	686 (161)	506 (94)	562 (187)	541 (201)	555 (312)	510 (117)	1058 (60)	1535 (111)	1566 (245)	2645 (393)
Mn	1837 (150)	1572 (187)	1814 (339)	1857 (158)	2038 (368)	1511 (155)	1847 (110)	2063 (129)	1487 (217)	1907 (272)
Co	194 (14)	188 (14)	202 (36)	201 (19)	220 (45)	179 (8)	277 (23)	311 (24)	254 (35)	297 (41)
Ni	702 (64)	695 (100)	740 (183)	644 (126)	599 (185)	606 (70)	904 (47)	733 (57)	1104 (149)	1106 (129)
Zn	674 (146)	526 (114)	600 (146)	762 (122)	715 (137)	507 (70)	1072 (245)	1072 (245)	809 (127)	918 (99)
Rh (ppb)	69 (13)	89 (18)	87 (34)	66 (15)	65 (38)	67 (9)	<2	<2	<2	<2
Ru	90 (9)	104 (21)	105 (36)	88 (16)	98 (31)	75 (25)	<10	<10	<10	<10
Ir	37 (35)	36 (43)	54 (38)	55 (47)	104 (76)	13 (15)	10 (2)	<4	<4	<4
Os	36 (9)	45 (9)	47 (16)	28 (7)	31 (22)	34 (11)	<4	<4	<4	<4
Ir/Ir^{*}[c]	0.8	0.7	0.9	1.5	2.2	0.3				

V, Mn, Ni and Zn concentrations in ppm, platinum group element concentrations in ppb; numbers in brackets represent one standard deviation (1σ).

[a] MgO_{WR} = MgO content (wt.%) in whole rock.

[b] n = number of separate grains analyzed.

[c] $Ir/Ir^{*} = Ir_N/(Ru_N \times Os_N)^{1/2}$.

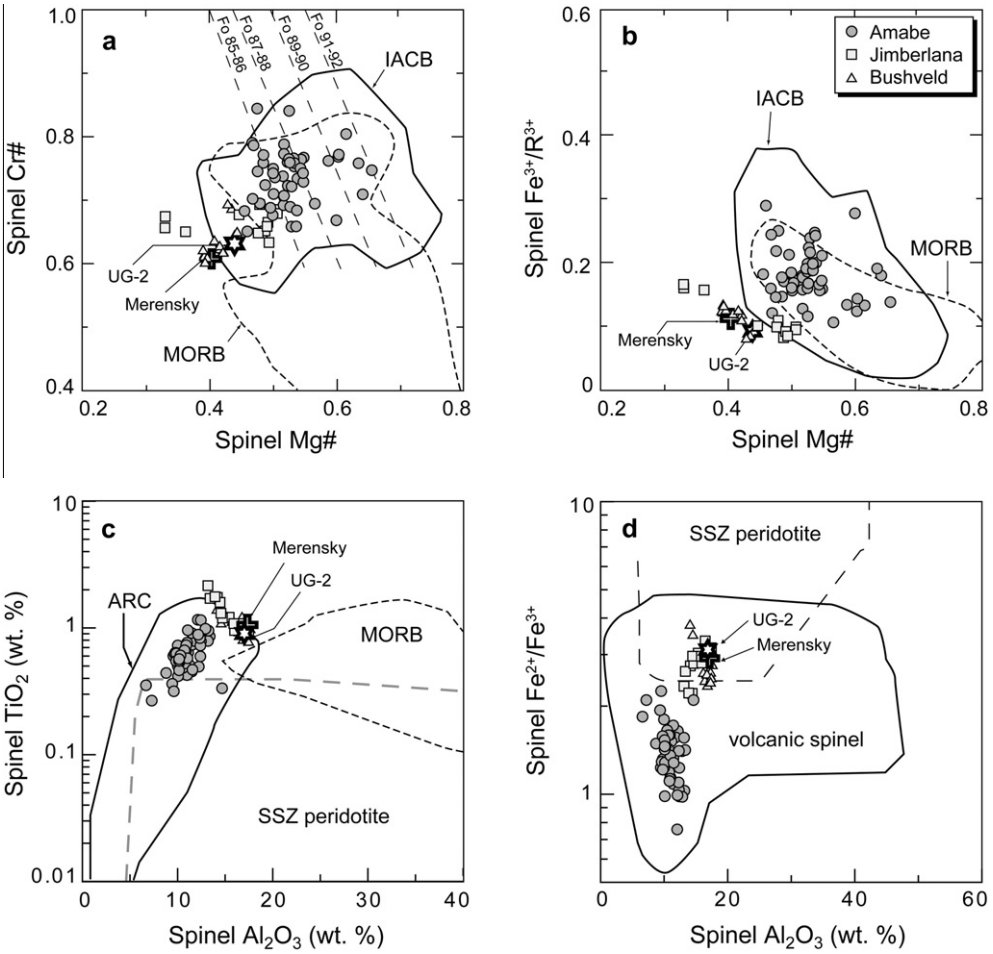

Fig. 5. (a and b) Binary plots of Mg# vs. Cr# and Fe^{3+}/R^{3+} ratio for the Ambae, Jimberlana and Bushveld Cr spinels (Mg# = Mg/(Mg + Fe^{2+}); Cr# = Cr/(Cr + Al); $Fe^{3+}/R^{3+} = Fe^{3+}/(Cr + Al + Fe^{3+})$). The fields (90th percentile) for island arc high-K calc-alkaline basalts (IACB) and mid ocean ridge basalts (MORB) are from Kamenetsky et al. (2001) and Barnes and Roeder (2001), respectively. Average composition of Cr spinels from UG2 chromitite and Merensky Reef are from Eales and Reynolds (1986). The isopleths of olivine Fo (dashed lines) are linear regression lines using olivine–Cr spinel data from modern submarine volcanic rocks (Kamenetsky et al., 2001). (c and d) Binary plots of Al_2O_3 vs. TiO_2 and Fe^{2+}/Fe^{3+} for the Ambae, Jimberlana and Bushveld Cr spinels. Fields for Cr spinels from island arc basalts (ARC), mid ocean ridge basalts (MORB) and supra subduction zone mantle (SSZ) are from Kamenetsky et al. (2001).

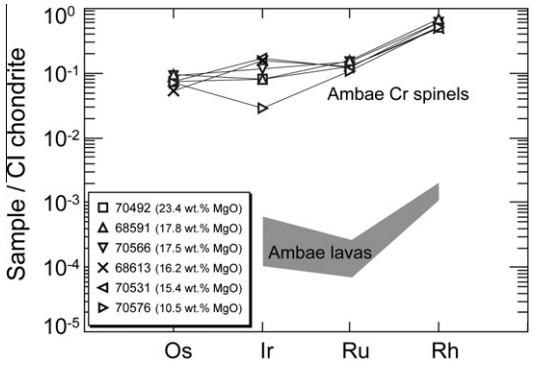

Fig. 6. CI-chondrite normalized PGE patterns for average Cr spinels in each sample from the Ambae lavas. Shaded area represents the whole rock PGE abundance in the Ambae lavas. Chondrite values from Anders and Grevesse (1989).

5. DISCUSSION

5.1. The enrichment of Rh and IPGEs in the Ambae Cr spinels

Our analyses of the Ambae Cr spinels show that they contain Rh and IPGEs at the tens of ppb level in solid solution and provide the first evidence from nature that these elements are highly compatible in Cr spinel when crystallized under oxidized conditions (fO_2 = QFM + 2.5). The results confirm the conclusions of experimental studies on various spinel species, including Cr spinel (Capobianco and Drake, 1990; Capobianco et al., 1994; Righter et al., 2004). In contrast, Cr spinels that crystallized under relatively reduced (~QFM) conditions, such as those from the Jimberlana layered intrusion and the Bushveld complex, contain at least one order of magnitude less Rh and IPGEs than the Ambae Cr spinels despite Rh and IPGE contents of the Bushveld and Jimberlana magmas (Keays and Campbell, 1981; Barnes and Maier, 2002) being at least 2–5 times higher than the Ambae arc picrite magmas (Fig. 1b).

The depletion in Rh and IPGEs in the Cr spinels from the Bushveld complex may be partly attributed to the presence of sulfide during their crystallization because when Cr spinel and sulfide melt coexist, the sulfide melt will dominate the PGE budget (Sattari et al., 2002). However, this cannot be the case for the Jimberlana Cr spinels because they have crystallized from a sulfide-undersaturated magma (Keays and Campbell, 1981). Therefore, the differences of Rh and IPGE abundances between the Ambae Cr spinels and the Jimberlana and Bushveld Cr spinels indicate that fO_2 is the principal factor that controls Rh and IPGE enrichment in Cr spinels.

The high compatibility of Rh and IPGE in Cr spinel under oxidized conditions can be attributed to changes in Cr spinel composition and structure with increasing fO_2, as previously shown for the transition metals (Burns, 1970). Site occupancies in spinel can be inferred from a combination of crystal chemistry (ionic radius and valences) and crystal field theory (Burns, 1970). Divalent ions with large octahedral site preference energy (e.g. Ni^{2+}) have a strong tendency to form inverse spinel such as magnetite (Burns, 1970). Barnes and co-workers (Barnes, 1998, 2000; Barnes and Brand, 1999), in their studies of Cr spinels from intrusive mafic and ultramafic rocks, found a linear correlation between the Ni and Fe^{3+} contents of Cr spinels. Because of its strong octahedral site preference, Ni partitions more strongly into Fe^{3+}-rich spinel which has a higher fraction of the inverse structure and therefore more divalent octahedral sites (Barnes, 1998). The positive correlation between Ni and Fe^{3+}/R^{3+} in the Ambae Cr spinel (Fig. 7f) indicates that an important factor controlling the Ni concentration in spinel is an increase in divalent octahedral sites with increasing fO_2. Vanadium, which also has a strong preference for the magnetite component in spinels, also increases with increasing Fe^{3+}/R^{3+} in the Ambae Cr spinels (Fig. 7e).

Previous experimental studies show that Rh and IPGEs have a strong preference for octahedral sites in the spinel structure (Capobianco and Drake, 1990; Capobianco, 1993; Nell and O'Neill, 1997; Righter and Downs, 2001; Brenan et al., 2011) in the low spin state (Geschwind and Remeika, 1962; Zhang et al., 2010). Among these elements, Rh and Ir are dominantly divalent for fO_2 between QFM and QFM + 2.5 (Borisov and Palme, 1995; Ertel et al., 1999) and have ionic radii in octahedral coordination (Rh^{2+} = 0.72 Å, Ir^{2+} = 0.74 Å; Shannon, 1976; Brenan et al., 2003) similar to Fe^{2+} (0.78 Å) and Mg^{2+} (0.72 Å), the cation they substitute for. Rh^{2+} and Ir^{2+} also have similar ionic radii to Ni^{2+} (0.69 Å; Shannon, 1976) but higher octahedral site preference energy in low spin state (Burns, 1970). Therefore, the behavior of Rh and Ir in Cr spinel is expected to be similar to Ni but the partition coefficients between Cr spinel and silicate melt should be even higher. The observed positive correlation between Rh and Ni contents in the Ambae Cr spinel is consistent with their expected similar crystal-chemical behavior (Fig. 8d). Furthermore, the Rh content in the Ambae Cr spinel increases with increasing spinel Fe^{3+}/R^{3+} (Fig. 7a), supporting the suggestion that the uptake of this element in Cr spinel from the melt is subject to the same crystal-chemical controls as Ni. However, Ir shows no correlation with Ni or Fe^{3+}/R^{3+} (Fig. 7d) indicating Ir substitution into Cr spinel is influenced by other factors.

The variation of Ru and Os in Cr spinels should not be controlled by the same mechanism as Ni and Rh because Ru and Os are dominantly trivalent for fO_2 between QFM and QFM + 3 (Borisov and Nachtweyh, 1998; Fortenfant et al., 2006). The high compatibility of Ru and Os in Cr spinel under oxidized condition is likely to be related to the changes in the oxidation state of these elements with fO_2. Ruthenium and Os are multivalent for fO_2 between QFM and QFM + 3 and the reduced species (mostly divalent) increase with decreasing oxygen fugacity (Borisov and Nachtweyh, 1998; Brenan et al., 2003, 2005). However, the magnetite component (i.e. divalent octahedral site) in Cr spinel decreases with decreasing fO_2, which lowers compatibility of the divalent Ru and Os into Cr spinel. There is also a compositional dependence of Ru partitioning in Cr spinel due to the difference in

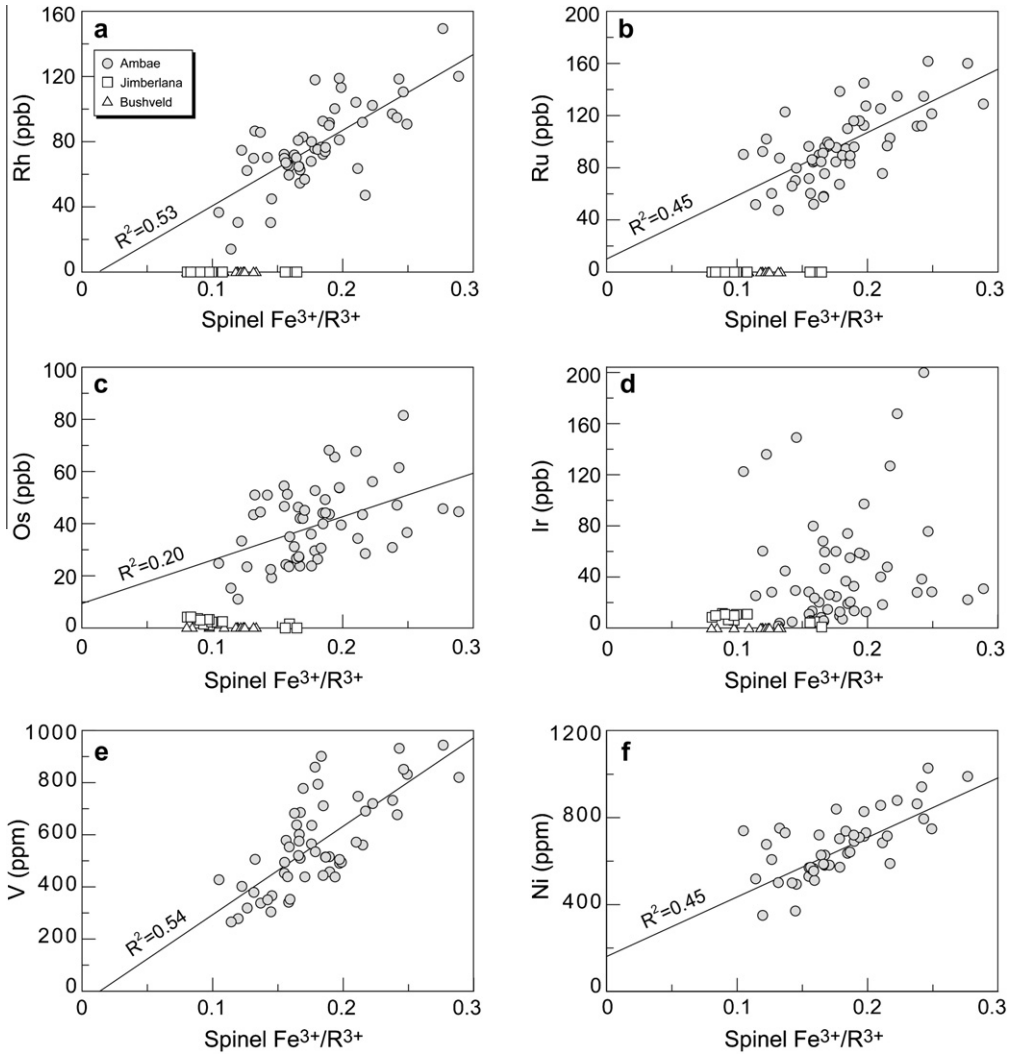

Fig. 7. Variation of (a) Rh, (b) Ru, (c) Os, (d) Ir, (e) V, and (f) Ni in the Ambae Cr spinels as a function of spinel Fe^{3+}/R^{3+}.

octahedral site preference energy between Fe^{3+} and Cr^{3+} (Brenan et al., 2011). Since the octahedral site preference energy for Cr^{3+} is much larger than Fe^{3+}, substitution of Ru^{3+} with Fe^{3+} provides higher stability than substitution of Ru^{3+} with Cr^{3+} (Brenan et al., 2011). The amount of Fe^{3+} in Cr spinel decreases with decreasing fO_2, which reduces the compatibility of Ru^{3+} into Cr spinel (Brenan et al., 2011). Os^{3+}, which has the same octahedral site preference energy as Ru^{3+} (Burns, 1970) and radii (0.68 Å; Shannon, 1976), will also have the same compositional dependence. As a consequence, the partition coefficients of Ru and Os are higher in high fO_2 melts than they are in low fO_2 melts.

To summarize, the correlations between Rh, Ru and Os with Fe^{3+}/R^{3+} in the Ambae spinels indicate that the combined effect of an increase in the fraction of the inverse structure in Cr spinels and the fraction of trivalent Ru and Os in the melt with increasing fO_2 in melts increases the partition coefficients of Rh and IPGEs into Cr spinels. Brenan et al. (2011) noted the importance of ferric iron in the spinel on the partitioning of PGE between Cr spinel and silicate melt. They also attributed the high partition coefficients for Rh and Ir at high oxygen fugacity to the strong affinity of these cations for divalent octahedral sites, and the increase in the partition coefficient for Ru with increasing oxygen fugacity to a change in melt speciation from Ru^{2+} to Ru^{3+} and preferential substitution of Ru^{3+} with Fe^{3+} in Cr spinel.

5.2. Origin of Pt–Fe alloys

Pt–Fe alloys containing varying amounts of Ir, Os and Rh occur as inclusions in some of the Ambae Cr spinels. Experimental studies on PGMs indicate that they crystallized at high temperature and are entrapped during growth of Cr spinels (Finnigan et al. 2008 and references therein), whereas Gijbels et al. (1974) and Capobianco et al. (1994) suggested that PGMs form by exsolution in plutonic Cr spinels during cooling. The Pt–Fe alloy inclusions in the Ambae Cr spinels cannot be the result of exsolution for two

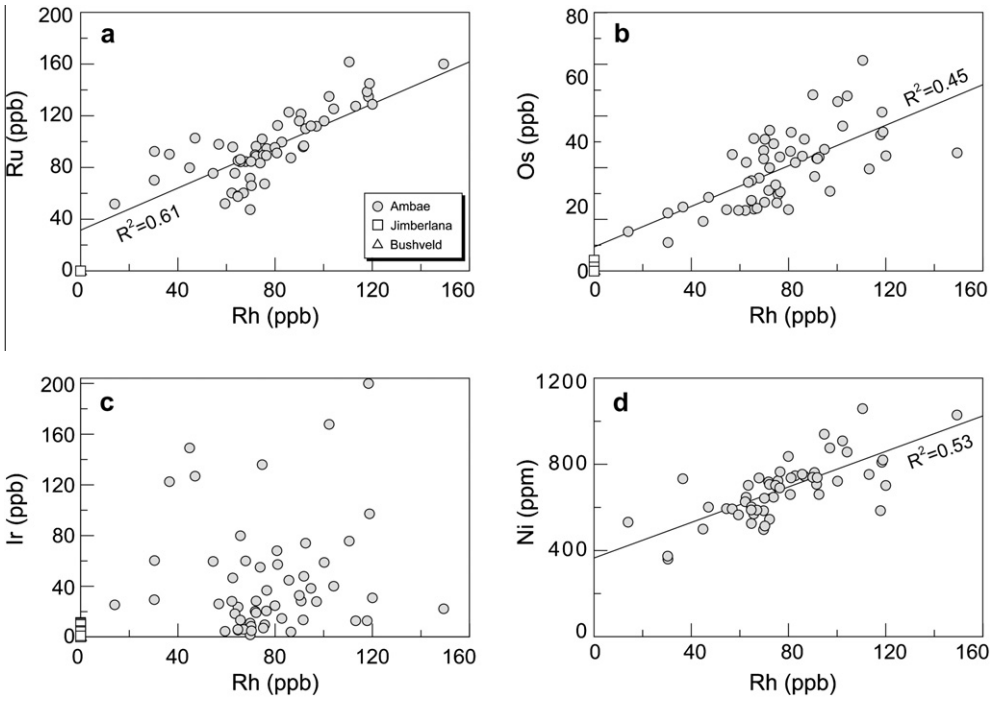

Fig. 8. Variation of (a) Ru, (b) Os, (c) Ir, and (d) Ni in Cr spinels from the Ambae lavas, the Jimberlana layered intrusion and the Bushveld complex as a function of Rh.

reasons: (i) the Ambae lavas cooled rapidly making exsolution unlikely and, (ii) Pt is strongly incompatible in Cr spinel (This study; Brenan et al., 2011). If a PGM phase did exsolve from the Ambae Cr spinels it would be rich in Ir, Os and Rh, the elements that enter the mineral structure, but not in Pt which is incompatible.

The formation of a Pt–Fe alloy phase results from the low solubility of Pt in silicate melts, which is a function of fO_2 and temperature (Borisov and Palme, 1997; Ertel et al., 1999; Fortenfant et al., 2003). The liquidus temperature of sample 68638 (aphyric lava; 10.7 wt.% MgO) is ~1170 °C according to the Petrologs program (Danyushevsky and Plechov, 2011) at 1 kbar and $fO_2 = \mathrm{QFM} + 2.5$ (Eggins, 1993). The estimated Pt solubility in a silicate melt under these condition is ~7 ppb (Fortenfant et al., 2003), which is slightly higher than the Pt content of sample 68638 (4.6 ppb). Alloy saturation will occur slightly before the magma becomes saturated with a pure Pt metal because the activity of Fe in the melt will promote the precipitation of a Pt–Fe alloy (Borisov and Palme, 2000). Similarly, Ir, Os and Rh will partition into the alloy, even though the concentration of these alloys is below that required for saturation of each element as the pure metal. Additional Ir, Os and Rh may partition into the alloys during subliquidus re-equilibrium as these elements are expelled from the cooling Cr spinels. Although it has been widely speculated that melts can become saturated with Pt–Fe alloys (e.g. Tredoux et al., 1995; Ballhaus and Sylvester, 2000), this study provides direct evidence for a magmatic origin of Pt–Fe alloys.

5.3. Variation of Rh and IPGE contents in Cr spinel below the liquidus

Composition of Cr spinel can be changed by re-equilibration with olivine and/or with the evolving melt during cooling (Irvine, 1967; Roeder and Campbell, 1985; Scowen et al., 1991; Kamenetsky et al., 2001). Of particular importance is the exchange of divalent Fe and Mg between Cr spinel, olivine and the melt, which depletes Mg and enriches Fe^{2+} in Cr spinel. In contrast to quenched submarine volcanic rocks (cooling rates of 100–100000 °C/h; Kamenetsky et al., 2001), thick subaerial lava flows such as the Ambae lavas have the cooling rates of 0.1–0.001 °C/h which provide sufficient time for the re-equilibration at near-magmatic temperatures (Kamenetsky et al., 2001). The extensive re-equilibration of Cr spinel with olivine is observed in several subaerial thick lava flows (Scowen et al., 1991; Barnes, 1998; Kamenetsky et al., 2001).

In the Ambae lavas, Cr spinel crystallization diminishes when Cr-bearing clinopyroxene (~0.4–0.7 wt.% Cr_2O_3) begins crystallizing along with olivine of Fo 89.4 (Eggins, 1993). The isopleths of olivine Fo in Fig. 5a are linear regression lines using olivine-spinel data from recent and modern submarine volcanic rocks (Kamenetsky et al., 2001). Consequently, most of the low Mg# Cr spinels (Mg# <0.60) from the Ambae lavas, which plot on the left-hand side of the Fo89–90 isopleths in Fig. 5a, can be interpreted to have significantly undergone subliquidus (between liquidus and solidus) re-equilibration. Re-equilibration may also continue under subsolidus conditions but at a slow rate. This conclusion is consistent with the enrichment of Zn and Mn in the low Mg# Cr spinels compared

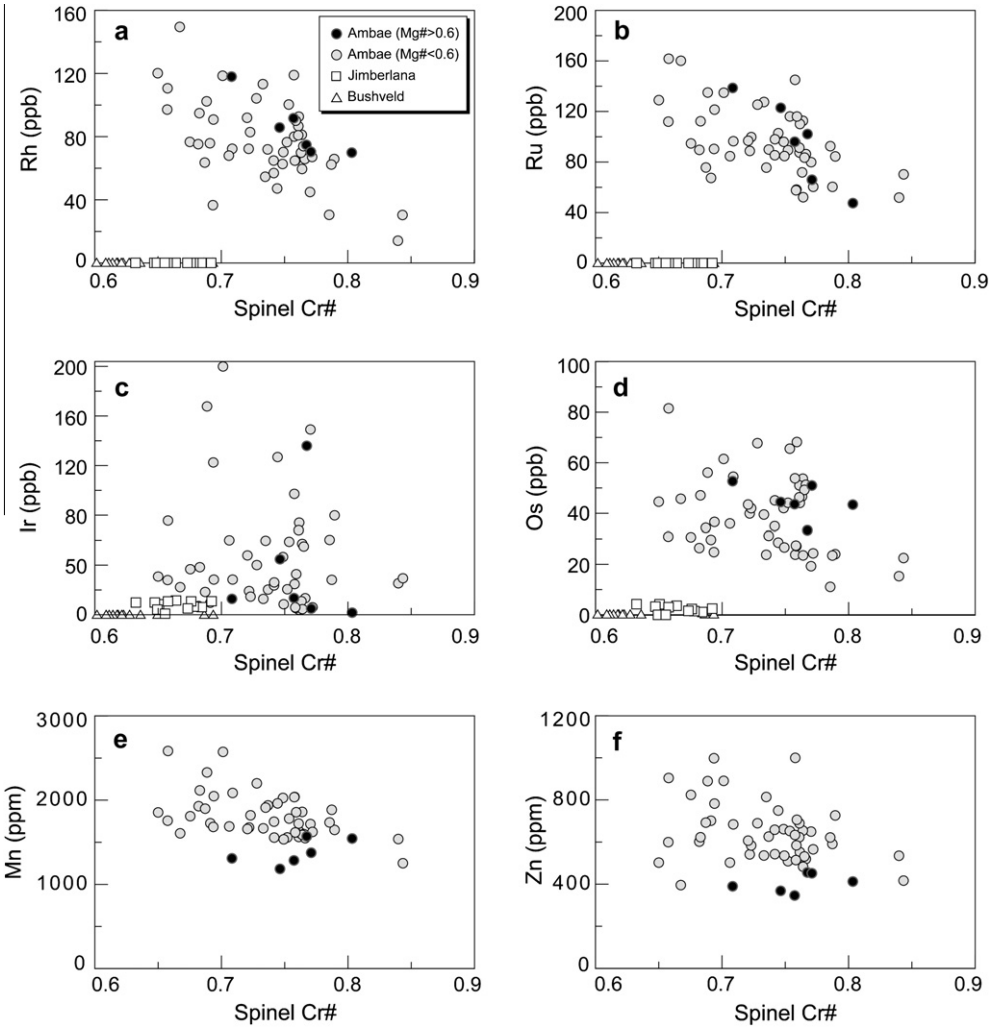

Fig. 9. Variation of (a) Rh, (b) Ru, (c) Ir, (d) Os, (e) Mn and (f) Zn in Cr-spinels from the Ambae lavas, the Jimberlana layered intrusion and the Bushveld complex as a function of spinel Cr#.

to the high Mg# spinels at a given Cr# (Fig. 9e and f). It suggests that these elements are added to the Cr spinel structure during sub-liquidus re-equlibration with olivine.

The low Mg# Cr spinels from the Ambae Lavas are slightly depleted in Rh, Ru and Os, compared to high Mg# Cr spinels at a given Cr# (Fig. 9a, b and d), indicating that the Ambae Cr spinels have lost some of these elements during cooling. One possible explanation for this trend is that PGEs, which were initially in solid solution in the Cr spinel, migrated to pre-existing PGMs as suggested by Gijbels et al. (1974). This suggestion is supported by the observation that the (Ir + Os)/Pt ratio of the alloys increases as the Mg# of the host Cr spinels decreases, indicating that Ir and Os were more enriched in the Pt–Fe alloys hosted by more slowly cooled Cr spinels (Fig. 4a). In contrast, the subliquidus re-equilibration between Cr spinel and Pt–Fe alloy appears to have had little influence on Rh and Ru in Cr spinel because Rh/Pt does not correlate with decreasing Mg# of the host Cr spinels and Ru is rarely hosted by Pt–Fe alloy from the Ambae lavas (Fig. 4b and Table A1).

5.4. The Cause of Ir variation

The concentration of Ir in the Ambae Cr spinels is highly variable compared with Rh, Ru and Os and does not show any correlation with Fe^{3+}/R^{3+}, V or Ni. The wide variation in the Ir contents of Cr spinels from a given sample may result from mixing of phenocrysts in the Ambae magma chamber because the compositional variation of the Ambae lavas with MgO > 9 wt.%, is controlled by addition and removal of olivine, clinopyroxene and Cr spinel (Eggins, 1993). For example mafic, crystal-rich lavas may contain a mixture of Cr spinels from less fractionated ($Ir/Ir^* > 1$) and more fractionated ($Ir/Ir^* < 1$) melts. Phenocryst mixing may explain much of the variability in the Ir concentration in Cr spinels from the same sample but it cannot explain why the concentration of Ir should vary appreciably more than the other IPGEs and Rh because phenocrysts mixing should affect all of these elements by similar amounts.

The large Ir variation relative to other IPGEs and Rh requires a mechanism that depletes the melt in Ir relative to other IPGEs and Rh. There is no obvious cause for this

depletion but we discuss two possibilities. The first is the effect of fractional crystallization of Pt–Fe alloys. The Pt–Fe alloys found in the Ambae lavas contain significantly higher Ir than Rh or Ru (Tables 4 and A1). Therefore, co-crystallization of Cr spinel and Ir-enriched Pt–Fe alloy could have more efficiently depleted the melt in Ir than Rh and Ru. However, if this were the case, Os should also show similar variability to Ir in Cr spinels because the Pt–Fe alloys from the Ambae lavas have similar concentrations of Os and Ir (Tables 4 and A1).

The second explanation is volatile loss of Ir. Clinopyroxene phenocrysts from the Ambae lavas show complex and abrupt compositional zoning patterns, which together with distinct populations of olivine phenocryst within the each lava, point to repeated magma mixing events that might be associated with redox changes induced by volatile degassing (Eggins, 1993). The volatile behavior of Ir during subaerial volcanic eruption has been reported in Hawaiian basalts (Zoller et al., 1983; Ireland et al., 2009; Pitcher et al., 2009). These studies show that the Ir content of some suites is more variable than the content of the other PGEs and this variability is attributed to volatile loss of Ir. However, there is no physical and chemical evidence for relatively high volatility of Ir to other PGEs.

5.5. Calculation of Cr spinel/silicate melt partition coefficient for Ti, Mn, Co, Ni, Zn, Ru, Rh and Ir

Cr spinel/silicate melt partition coefficients can be calculated using trace element and PGE abundances of sample 68638 (aphyric lava; 10.7 wt.% MgO) and their concentrations in the equilibrium Cr spinels. Since all Ambae lavas investigated in this study have accumulated early formed Cr spinels, the best way to constrain the equilibrium Cr spinel composition is to use the compositional relationship between the host olivine and the Cr spinel. Fig. 10 shows the relationship between host olivine Fo and spinel Mg#, Cr^{3+}/R^{3+} and Fe^{3+}/R^{3+} using olivine-spinel pairs that yield the highest temperatures (>1050°C) and have therefore undergone the least re-equilibration. We have used this approach to estimate the equilibrium Cr spinel composition. Assuming equilibrium Fe/Mg partitioning between basaltic liquid and olivine ($K_D^{Fe/Mg}{}_{ol\text{-}melt} = 0.3$; Roeder and Emslie, 1970) and $X_{Fe_2O_3}/X_{FeO} = 0.28$ at $fO_2 = QFM + 2.5$ calculated from the equation of Kilinc et al. (1983), the olivine in equilibrium with melt (sample 68638) has a composition of Fo 90.9. The compositions of Cr spinels, hosted by olivines with similar Fo ($90.7 < Fo < 91.1$), have Mg# values of 0.62–0.66, Cr^{3+}/R^{3+} of 0.56–0.67 and Fe^{3+}/R^{3+} of 0.12–0.20 (Fig. 10). This compositional range is consistent with the Cr spinel composition calculated from the computational program SPINMELT (Ariskin and Nikolaev, 1996). According to this program, the Cr spinel in equilibrium with melt composition (sample 68638) has Mg# = 0.63, $Cr^{3+}/R^{3+} = 0.60$ and $Fe^{3+}/R^{3+} = 0.11$ at 1200 °C and fO_2 of QFM + 2.5. The average Ti, Mn, Co, Ni, Zn, Ru, Rh and Ir concentrations in the Ambae Cr spinels ($n = 3$; 68576-H03, 70591-H02 and 70591-H03), which have Mg#, Cr^{3+}/R^{3+} and Fe^{3+}/R^{3+} within these ranges, are reported in Table 7. Using these values and Ti, Mn, Co, Ni, Zn, Ru, Rh and Ir concentrations in sample 68638 (Table 3), we calculated the empirical Cr spinel/silicate melt partition coefficients at 1170 °C and fO_2 of QFM + 2.5. The partition coefficients for Ti, Mn, Co, Ni and Zn are consistent with the previously determined values (Table 7), suggesting that equilibrium has been attained between the selected Cr spinels and the aphyric lava.

All the published D_{Ir}, D_{Ru} and D_{Rh} are compiled in Table 7 and Fig. 11. The calculated partition coefficients for Ir and Ru ($D_{Ir} \sim 470$ and $D_{Ru} \sim 2450$) are similar to those obtained by experiments performed at high oxygen fugacity ($fO_2 > QFM + 2$). D_{Ir} and D_{Ru} increase with increasing fO_2 in silicate melts at fO_2 between QMF–2 and QMF + 3 (Fig. 11), showing their dependency on oxygen fugacity. The correlation between D_{Ru} and oxygen fugacity

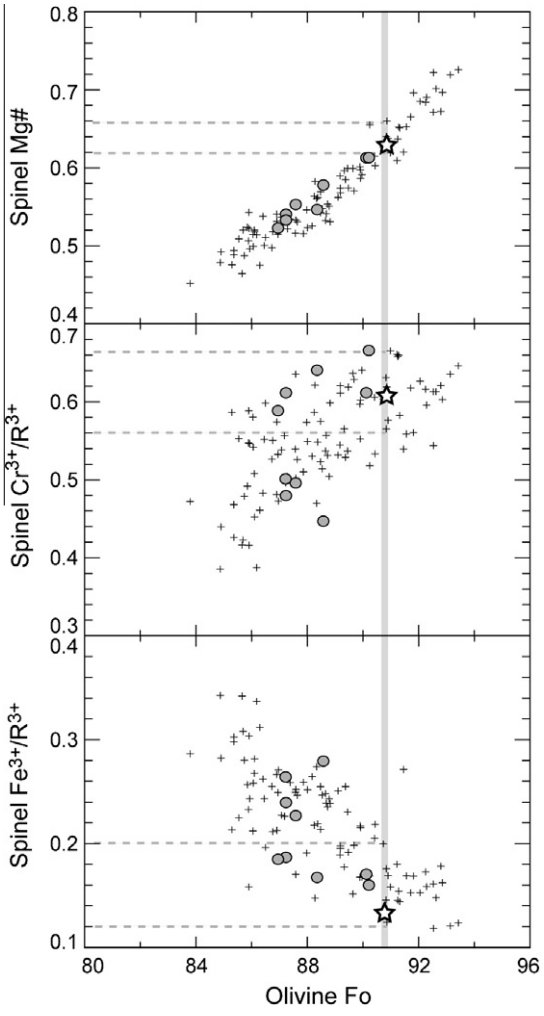

Fig. 10. Variation of spinel Mg#, Cr^{3+}/R^{3+} and Fe^{3+}/R^{3+} from the Ambae Cr spinels as a function of the host olivine Fo. Filled circles are from this study. Crosses are the Ambae olivine–Cr spinel data from Kamenetsky et al. (2001) that yield the highest temperatures (>1050 °C). Stars are the Cr spinel composition calculated by SPINMELT (Ariskin and Nikolaev, 1996). The gray shaded areas show olivine with $90.7 < Fo < 91.1$. Dashed lines represent the compositional range of Cr spinels in equilibrium with olivine with $90.7 < Fo < 91.1$.

Table 7
Empirical partition coefficients of Ti, Mn, Co, Ni, Zn, Rh, Ru and Ir.

Parameter	Ti	Mn	Co	Ni	Zn	Rh	Ru	Ir
Concentrations								
$C^{liquid,\ a}$	4605	1194	42.0	146	53.5	0.154	0.05 (0.02)	0.050
$C^{Cr\ spinel,\ b}$	3587	1258	174	682	370	98 (17)	119 (22)	24 (18)
Partition coefficients								
$D^{Cr\ spinel}$	0.78	1.1	4.1	4.7	6.9	641 (112)	2448 (1533)	472 (364)
Literature values	0.34–0.91	0.88–1.11	3.8–8.3	1.3–6.8	3.6–10.1	0.04–530	2.9–1143	0.16–22000
Reference	1	1	1, 2	1, 3	1, 2	4	4, 5	4, 5

Ti, Mn, Co, Ni and Zn concentrations are in ppm and Rh, Ru and Ir concentrations are in ppb.
[a] Ti, Mn, Co, Ni, Zn, Rh, Ru and Ir concentrations in an aphyric lava (68638).
[b] Average of analyses of three Cr spinels (68576-H03, 70591-H02, 70591-H03) from Table A4. Reference: 1 = Pagé and Barnes (2009), 2 = Horn et al. (1994), 3 = Sattari et al. (2002), 4 = Brenan et al. (2011) and Righter et al. (2004), 5 = Puchtel and Humayun (2001) and Pagé et al. (2011).

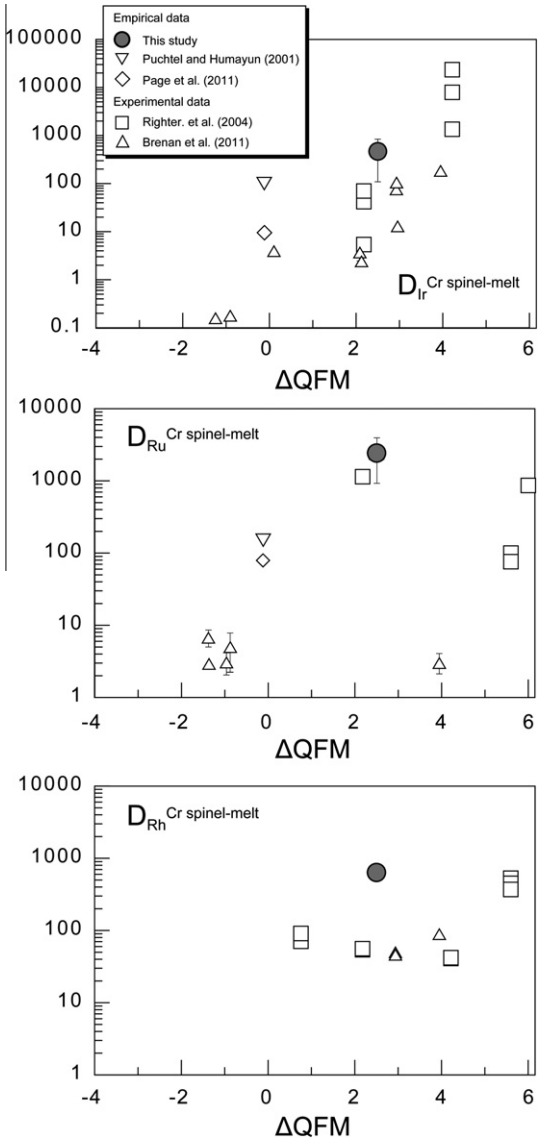

Fig. 11. Summary of empirical and experimental data for Cr spinel-melt partitioning for Ir, Ru and Rh. Filled circles show data from this study. Unfilled symbols are taken from the literatures.

does not extend to $fO_2 > QMF + 3$, which suggests a valence change in Ru from 3+ to 4+ across the fO_2 range (Righter et al., 2004). The uncertainty introduced by the NiAr interference correction on Ru in whole rock and Cr spinels has been taken as the full magnitude of the correction, which is the maximum possibility of the error. D_{Rh} obtained in this study ($D_{Rh} \sim 640$) is a factor of 10 higher than those of Righter et al. (2004) at fO_2 of QFM + 2.2 ($D_{Rh} = 54$–56). Additional studies are therefore required to clarify the correct partition coefficient for Rh in Cr spinel.

Simple mass balance calculations were carried out to determine the percentage of Rh, Ru and Ir held in Cr spinel using the Rh, Ru and Ir concentrations of the whole rock and Cr spinel, and the weight fraction of Cr spinel in each sample (Tables 3, 5 and A2). The results show that 10–37% of the Ir, 30–100% of the Ru and 10–60% of the Rh are held in Cr spinels. Cr spinel clearly has an important influence on the geochemistry and behavior of these elements, especially Ru, during fractional crystallization of the Ambae magma.

6. CONCLUSIONS

Cr spinels from the oxidized Ambae lavas are enriched in Rh and IPGEs relative to the Cr spinels that crystallize from the more reduced Jimberlana layered intrusion and Bushveld complex. Our results provide the first natural evidence that these elements are highly compatible in Cr spinels under oxidizing condition ($fO_2 = QFM + 2.5$), as predicted from experimental studies on various spinel species, including Cr spinel (Capobianco and Drake, 1990; Capobianco et al., 1994; Righter et al., 2004). The enrichment of Rh and IPGEs in the Ambae Cr spinels is a result of the fO_2 dependency of partition coefficients for Rh and IPGEs between Cr spinel and silicate melt. The correlations between Rh, Ru and Os with Fe^{3+}/R^{3+}, V and Ni in the Ambae Cr spinels indicate that the increase in the partition coefficients of Rh and IPGEs with fO_2 can be attributed to the combined effect of an increase in the fraction of the inverse structure in Cr spinels and the fraction of trivalent Ru and Os in

the melt. Partition coefficients for Rh, Ru and Ir between Cr spinel and silicate melt are ~640, ~2450 and ~470, respectively at ca. 1170 °C and fO_2 of QFM + 2.5. These values, together with values taken from the literature, show that partitioning of Ru and Ir into Cr spinel increases with increasing fO_2 in silicate melts. Our results show that Cr spinel may play an important role in the fractionation of Rh, Ru, Ir and Os during the evolution of mantle-derived magma and mantle partial melting in oxidized environments.

ACKNOWLEDGEMENTS

This research is funded by a grant from ARC Discovery grant to Ian Campbell. We thank Charllote Allen for assistance with the LA-ICP-MS analysis and valuable comments. Robert Rapp and Frank Blink provided assistance with the electron microprobe analyses and back scattered electron imaging. We also thank Hugh O'Neill and Vadim Kamenetsky for their constructive comments and discussion. Kari Kojonen provided the Bushveld chromitite samples. PGE glass standard were kindly provided by Guilherme Mallmann. This paper benefited greatly from reviews by James Brenan, Chris Dale and an anonymous reviewer. We also thank Mark Rehkämper for the editorial handing.

APPENDIX A. Pt–Fe ALLOY COMPOSITION

The compositions of Pt–Fe alloy inclusions observed in LA-ICP-MS time resolved spectra were quantified using the method described in Halter et al. (2002). The analytical signals of the host Cr spinel and the host plus Pt–Fe alloy inclusion mixture were converted into element concentrations using element sensitivity factors and Ti concentration in Cr spinel determined by electron micro-

Table A1
Calculated compositions of Pt–Fe alloys from the Ambae lavas by LA-ICP-MS analysis (wt.%).

Cr spinel host		Alloy						
Sample	Spinel Mg#	Pt	Rh	Ir	Os	Total	(Ir + Os)/Pt	Rh/Pt
70492-Cr-3	0.460	80	0.8	6	5	91.4	0.13	0.011
	0.460	80	1.0	21	26	128.2	0.59	0.012
	0.460	80	0.7	8	6	94.8	0.18	0.009
	0.460	80	0.6	7	8	95.1	0.18	0.007
68613-H04	0.479	80	0.6	8	7	95.8	0.19	0.007
68613-A20	0.502	80	1.9	15	13	110.0	0.35	0.024
68591-A05	0.520	80	1.6	8	4	93.7	0.15	0.020
70566-A02	0.599	90	1.5	4	3	99.1	0.08	0.016
68613-A21	0.640	90	0.9	1	4	96.7	0.06	0.010

The calculation procedure is described in Appendix A.

Table A2
Modal analyses of the selected Ambae lavas and Cr contents in each phase.

	70531		70566		70492	
	Mode (wt.%)	Cr (ppm)	Mode (wt.%)	Cr (ppm)	Mode (wt.%)	Cr (ppm)
Phenocryst						
Olivine	19.3	209	19.4	308	35.4	365
Clinopyroxene	17.9	3163	8.7	4580	0.5	3668
Cr spinel[a]	0.028	275051	0.092	344616	0.223	305674
Groundmass						
Olivine	3.3	–	–	–	2.9	–
Augite	19.0	494	29.2	967	23.8	2785
Ti–Fe oxide	1.8	796	1.7	3777	2.3	1616
Plagioclase and undifferentiated part	38.6	–	40.9	–	34.8	–

The weight percentage of Cr spinel in each sample was calculated using the Cr contents of the spinel and the whole rock, after subtracting the Cr in held the phenocrysts (olivine, augite and Fe–Ti- spinel) and groundmass: $F_{\text{Cr-spinel}} = (\text{Cr}_{\text{wholerock}} - F_{\text{phenocryst}} \times \text{Cr}_{\text{phenocryst}} - F_{\text{matrix}} \times \text{Cr}_{\text{matrix}})/\text{Cr}_{\text{Cr spinel}}$. Where, F_A is weight fraction of phase A and Cr_A is an average Cr content of phase A.

[a] Calculated percentage of Cr spinel = $F_{\text{Cr spinel}} \times 100$.

Table A3
Major element contents in Cr spinels from the Ambae lavas, the Jimberlana intrusion and the Bushveld complex (wt.%).

Sample no.	Cr_2O_3	Al_2O_3	TiO_2	FeO [a]	Fe_2O_3 [a]	MgO	Total	Mg# [b]	Cr# [c]	Cr^{3+}/R^{3+}, [d]	Fe^{3+}/R^{3+}, [e]
Ambae lavas											
70492 (23.4 wt.% MgO)											
70492-A23	46.5	10.5	0.66	18.2	13.1	10.2	99.2	0.500	0.749	0.623	0.167
70492-A26	49.3	14.6	0.33	16.5	8.8	12.0	101.6	0.565	0.694	0.621	0.105
70492-A27	46.2	11.1	0.64	17.6	12.8	10.5	98.8	0.515	0.737	0.617	0.163
70492-A37	42.8	12.8	0.84	17.9	14.1	10.7	99.3	0.516	0.691	0.568	0.179
70492-A39	41.3	13.3	0.85	18.4	14.4	10.3	98.6	0.499	0.675	0.552	0.183
70492-cr-1	44.4	11.5	0.73	17.6	14.6	10.8	99.6	0.523	0.722	0.588	0.185
70492-cr-2	45.9	11.8	0.78	19.2	13.6	10.2	101.6	0.487	0.723	0.600	0.169
70492-cr-5	44.2	12.3	0.59	17.8	14.0	10.7	99.6	0.517	0.706	0.582	0.176
70492-cr-6	42.0	13.1	0.79	20.1	14.3	9.4	99.6	0.454	0.682	0.559	0.181
70492-H02	46.9	12.2	0.49	19.7	10.6	9.3	99.2	0.500	0.709	0.599	0.155
Average	45.0	12.3	0.67	18.3	13.0	10.4	99.7	0.508	0.709	0.591	0.166
SD (1σ)	2.5	1.2	0.16	1.1	1.9	0.8	1.1				
68591 (17.8 wt.% MgO)											
68591-A03	45.8	9.5	0.60	17.3	15.5	10.7	99.4	0.524	0.764	0.613	0.197
68591-A08	51.6	10.5	0.48	14.7	9.9	12.5	99.7	0.602	0.767	0.673	0.122
68591-A09	37.7	13.2	0.95	17.5	18.8	11.0	100.5	0.528	0.657	0.501	0.238
68591-A10	50.9	10.7	0.52	15.4	10.7	12.3	100.2	0.587	0.761	0.660	0.133
68591-H01	48.7	10.0	0.50	16.5	12.5	11.2	99.6	0.548	0.766	0.646	0.157
68591-H02	44.7	12.3	0.72	13.5	14.4	13.5	99.3	0.641	0.708	0.582	0.179
68591-H03	47.1	10.1	0.61	13.6	15.3	13.3	99.7	0.634	0.757	0.614	0.190
68591-H04	48.6	10.1	0.53	16.6	12.3	11.1	99.0	0.544	0.763	0.645	0.155
68591-H05	44.3	10.8	0.65	16.9	15.7	11.1	99.8	0.538	0.733	0.587	0.199
Average	46.6	10.8	0.62	15.8	13.9	11.8	99.7	0.572	0.742	0.613	0.174
SD (1σ)	4.2	1.2	0.15	1.5	2.8	1.1	0.5				
70566 (17.5 wt.% MgO)											
70566-A01	45.6	10.0	0.60	17.0	15.3	10.9	99.4	0.533	0.753	0.607	0.194
70566-A02	36.1	12.1	1.15	14.9	21.7	12.5	98.5	0.599	0.667	0.483	0.277
70566-A05	45.3	9.6	0.62	17.1	14.7	10.5	97.9	0.522	0.759	0.615	0.190
70566-A13	40.5	12.3	0.83	17.6	17.7	11.0	99.9	0.526	0.689	0.535	0.223
70566-A17	42.1	10.9	0.76	17.2	16.8	10.8	98.6	0.529	0.721	0.566	0.215
70566-cr-8	47.8	10.1	0.58	17.3	13.1	10.8	99.7	0.526	0.761	0.635	0.166
70566-cr-10	34.3	12.4	1.14	20.0	22.5	9.5	99.9	0.459	0.650	0.462	0.289
70566-cr-13	45.9	10.2	0.63	17.1	14.7	10.9	99.5	0.533	0.752	0.612	0.187
70566-H01	46.7	9.8	0.59	17.4	14.6	10.7	99.8	0.524	0.761	0.621	0.185
70566-H02	56.6	7.2	0.27	17.2	9.1	10.7	101.1	0.525	0.840	0.744	0.114
70566-H03	47.2	9.7	0.63	17.2	14.8	11.0	100.6	0.532	0.765	0.622	0.187
70566-H05	53.3	6.6	0.35	18.6	11.2	9.4	99.6	0.474	0.843	0.721	0.145
70566-1	43.3	10.9	0.73	16.7	16.6	11.3	99.5	0.547	0.728	0.575	0.210
70566-2	36.9	12.9	0.98	17.1	19.3	11.1	98.1	0.536	0.658	0.496	0.246
70566-3	38.9	12.1	0.88	17.1	19.0	11.1	99.1	0.537	0.683	0.518	0.242
70566-6	53.3	8.8	0.44	14.2	10.6	12.7	99.9	0.614	0.803	0.698	0.132
70566-7	45.7	9.8	0.63	17.1	15.6	10.9	99.7	0.533	0.758	0.608	0.197
Average	44.7	10.3	0.69	17.1	15.7	10.9	99.5	0.532	0.741	0.595	0.200
SD (1σ)	6.2	1.7	0.25	1.2	3.6	0.8	0.8				
68613 (16.2 wt.% MgO)											
68613-A02	46.6	10.0	0.56	18.6	13.8	9.8	99.5	0.484	0.758	0.624	0.176
68613-A19	48.2	11.4	0.45	18.3	11.1	10.2	99.7	0.467	0.789	0.664	0.158
68613-A20	46.1	11.2	0.51	18.1	13.2	10.3	99.4	0.502	0.735	0.612	0.167
68613-H01	46.8	10.9	0.42	18.1	12.6	10.1	98.9	0.499	0.742	0.623	0.159
68613-H02	40.6	12.4	0.78	18.5	16.6	10.2	99.1	0.495	0.687	0.542	0.211
68613-H03	50.0	10.0	0.41	18.8	11.6	9.9	100.8	0.484	0.770	0.658	0.145
68613-H04	38.6	11.4	0.91	19.0	19.4	9.8	99.2	0.479	0.694	0.521	0.249
Average	45.3	11.0	0.58	18.5	14.0	10.0	99.5	0.487	0.739	0.606	0.181
SD (1σ)	4.1	0.9	0.19	0.4	3.0	0.2	0.6				

(*continued on next page*)

Table A3 (*continued*)

Sample no.	Cr_2O_3	Al_2O_3	TiO_2	FeO [a]	Fe_2O_3 [a]	MgO	Total	Mg# [b]	Cr# [c]	Cr^{3+}/R^{3+}, [d]	Fe^{3+}/R^{3+}, [e]
70531 (15.4 wt.% MgO)											
70531-A01	38.6	11.0	0.95	19.1	18.6	9.4	97.6	0.467	0.701	0.531	0.243
70531-A08	51.8	9.4	0.36	17.5	10.0	10.5	99.5	0.517	0.787	0.687	0.127
70531-A10	43.3	10.0	0.72	19.0	16.9	9.7	99.6	0.475	0.744	0.583	0.217
70531-H02	52.2	9.6	0.32	19.2	9.5	9.5	100.2	0.469	0.785	0.691	0.120
Average	46.4	10.0	0.59	18.7	13.7	9.8	99.2	0.482	0.755	0.623	0.177
SD (1σ)	6.7	0.7	0.30	0.8	4.7	0.5	1.1				
70576 (10.5 wt.% MgO)											
70576-H01	47.5	10.7	0.66	16.9	13.1	11.2	100.1	0.543	0.749	0.626	0.164
70576-H02	47.0	11.0	0.57	16.7	13.4	11.3	100.1	0.547	0.742	0.615	0.171
70576-H04	48.1	10.2	0.60	17.5	13.3	10.9	100.6	0.526	0.759	0.632	0.166
70576-H05	50.5	11.5	0.47	13.0	11.3	13.9	100.6	0.655	0.746	0.644	0.137
70576-H06	49.4	9.8	0.55	17.7	12.5	10.6	100.6	0.517	0.772	0.651	0.156
70576-H07	50.7	10.1	0.46	14.7	11.5	12.5	99.9	0.603	0.771	0.661	0.142
70576-H08	48.7	10.1	0.55	17.4	12.6	10.8	100.2	0.524	0.764	0.643	0.159
70576-H09	47.3	10.1	0.57	17.2	13.1	10.7	98.9	0.526	0.758	0.632	0.166
Average	48.7	10.4	0.55	16.4	12.6	11.5	100.1	0.555	0.758	0.638	0.158
SD (1σ)	1.4	0.6	0.07	1.7	0.8	1.1	0.5				
Jimberlana intrusion											
BRD11											
BRD11-190-1	45.3	15.4	1.21	19.0	7.0	10.3	98.1	0.491	0.664	0.605	0.089
BRD11-190-2	45.6	14.1	1.73	18.7	7.6	10.8	98.5	0.506	0.684	0.618	0.098
BRD11-190-3	44.8	13.3	1.70	19.4	8.2	10.0	97.4	0.478	0.692	0.618	0.108
BRD11-190-4	46.0	14.6	1.19	18.5	7.3	10.6	98.3	0.506	0.678	0.615	0.093
BRD11-190-5	45.1	14.5	1.30	20.6	7.7	9.3	98.5	0.446	0.676	0.609	0.100
BRD11-260-1	45.6	16.4	1.07	19.4	6.5	10.3	99.4	0.487	0.651	0.598	0.081
BRD11-260-2	43.6	15.9	0.95	19.3	7.7	9.8	97.2	0.476	0.647	0.584	0.098
BRD11-260-3	45.4	15.8	1.08	19.2	7.2	10.4	99.2	0.490	0.658	0.598	0.091
BRD11-260-4	44.6	17.4	0.89	19.2	6.8	10.5	99.3	0.493	0.632	0.580	0.084
Average	45.1	15.3	1.23	19.3	7.3	10.2	98.4	0.486	0.665	0.603	0.093
SD (1σ)	0.7	1.3	0.30	0.6	0.5	0.4	0.8				
NDDI-830-2	39.8	14.4	1.58	23.6	11.9	7.5	98.8	0.361	0.649	0.548	0.156
NDDI-830-3	39.4	13.9	1.75	24.8	12.4	6.8	99.1	0.329	0.656	0.547	0.165
Average	39.6	14.1	1.67	24.2	12.2	7.2	98.9	0.345	0.652	0.548	0.160
SD (1σ)	0.3	0.4	0.12	0.8	0.4	0.5	0.2				
Bushveld complex											
UG2											
UG2-3-1	41.1	16.7	1.22	21.9	9.4	8.7	99.1	0.416	0.623	0.548	0.120
UG2-3-2	42.1	16.2	1.03	22.1	9.4	8.5	99.3	0.407	0.636	0.560	0.119
UG2-3-3	41.5	17.2	1.00	21.7	9.4	8.9	99.7	0.421	0.618	0.545	0.118
UG2-3-4	41.1	16.4	0.93	21.6	9.8	8.6	98.4	0.415	0.627	0.549	0.124
UG2-3-5	42.2	17.5	0.98	21.9	8.8	8.9	100.5	0.421	0.617	0.550	0.109
UG2-5-1	39.9	16.8	0.81	22.3	10.5	8.1	98.4	0.392	0.614	0.532	0.134
UG2-5-2	40.5	17.3	1.00	22.7	9.7	8.2	99.4	0.391	0.611	0.537	0.122
UG2-5-3	40.9	16.7	0.93	22.6	9.7	8.1	99.0	0.389	0.621	0.545	0.124
UG2-5-4	40.4	17.4	0.78	22.4	9.9	8.2	99.1	0.396	0.609	0.533	0.125
UG2-5-5	38.9	17.3	1.04	22.4	10.3	8.1	98.1	0.392	0.602	0.522	0.132
Average	40.9	16.9	0.97	22.2	9.7	8.4	99.1	0.404	0.618	0.542	0.123
SD (1σ)	1.0	0.5	0.12	0.4	0.5	0.3	0.7				
Merensky reef											
Mrimp-1	43.3	15.7	1.12	20.5	7.6	9.1	97.3	0.443	0.650	0.586	0.098
Mrimp-2	47.4	14.5	1.09	21.2	6.7	9.1	100.0	0.434	0.686	0.628	0.085
Mrimp-3	47.5	14.1	1.40	21.5	6.3	9.0	99.7	0.428	0.694	0.638	0.080
Average	46.0	14.7	1.20	21.1	6.9	9.1	99.0	0.435	0.677	0.617	0.088
SD (1σ)	2.4	0.8	0.17	0.5	0.7	0.1	1.5				

Data were measured by EPMA.

[a] FeO and Fe_2O_3 are obtained by stoichiometric calculations using equations of Murck and Campbell (1986).

[b] $Mg\# = Mg/(Fe^{2+} + Mg)$.

[c] $Cr\# = Cr/(Cr + Al)$.

[d] $Cr^{3+}/R^{3+} = Cr/(Cr + Al + Fe^{3+})$.

[e] $Fe^{3+}/R^{3+} = Fe^{3+}/(Cr + Al + Fe^{3+})$.

Table A4
Trace element and PGE contents in Cr spinels from the Ambae lavas, the Jimberlana layered intrusion and the Bushveld complex.

Sample no.	V (ppm)	Mn (ppm)	Co (ppm)	Ni (ppm)	Zn (ppm)	Rh (ppb)		Ru (ppb)	Ir (ppb)	Os (ppb)	Ir/Ir^{*}, [a]	Ir_N/Ru_N
Ambae lavas												
70492 (23.4 wt.% MgO)												
70492-A23	686	2026	201	647	663	63	(55)	96	47	42	0.9	0.7
70492-A26	428	1681	221	733	999	37	(32)	90	123	25	3.2	2.0
70492-A27	683	1937	209	718	628	72	(66)	90	20	31	0.5	0.3
70492-A37	860	1725	192	723	703	76	(71)	67	10	30	0.3	0.2
70492-A39	901	1809	195	765	825	77	(73)	95	37	31	0.8	0.6
70492-cr-1	711	1674	179	707	543	72	(71)	89	19	40	0.4	0.3
70492-cr-2	778	1819	203	747	585	83	(84)	100	15	42	0.3	0.2
70492-cr-5	565	1687	185	736	504	68	(74)	85	60	36	1.3	1.1
70492-cr-6	794	1927	181	697	603	75	(70)	90	7	26	0.2	0.1
70492-H02	453	2085	177	545	685	72	(69)	96	28	54	0.5	0.4
Average	686	1837	194	702	674	69		90	37	36	0.8	0.6
SD (1σ)	161	150	14	64	146	13		9	35	9		
68591 (17.8 wt.% MgO)												
68591-A03	491	1860	210	737	656	81	(76)	113	57	54	0.9	0.8
68591-A08	402	1569	186	703	457	75	(69)	102	136	33	2.8	2.0
68591-A09	732	1755	200	876	601	97	(90)	112	28	31	0.6	0.4
68591-A10	506	1562	205	746	690	87	(72)	87	<4	51	<0.1	<0.1
68591-H01	439	1548	167	569	521	66	(61)	86	13	51	0.2	0.2
68591-H02	535	1308	179	585	391	118	(109)	139	13	53	0.2	0.1
68591-H03	458	1284	175	707	348	92	(82)	96	13	44	0.3	0.2
68591-H04	495	1596	179	585	530	70	(62)	72	11	47	0.2	0.2
68591-H05	495	1665	189	753	538	113	(100)	127	13	40	0.2	0.1
Average	506	1572	188	695	526	89		104	36	45	0.7	0.5
SD (1σ)	94	187	14	100	114	18		21	43	9		
70566 (17.5 wt.% MgO)												
70566-A01	439	1780	201	722	654	100	(94)	116	59	66	0.7	0.8
70566-A02	944	1605	211	1029	397	149	(136)	160	22	46	0.3	0.2
70566-A05	516	1856	209	740	707	90	(85)	57	16	34	0.5	0.4
70566-A13	720	2328	262	909	891	102	(96)	135	168	56	2.4	1.8
70566-A17	561	1657	187	738	608	92	(85)	97	48	43	0.9	0.7
70566-cr-8	521	1721	183	660	625	81	(83)	91	68	46	1.3	1.1
70566-cr-10	820	1854	184	702	504	120	(125)	129	31	45	0.5	0.4
70566-cr-13	514	1557	179	691	511	76	(77)	89	21	44	0.4	0.3
70566-H01	444	1627	176	660	553	93	(85)	110	74	44	1.3	1.0
70566-H02	266	1538	168	531	536	14	(13)	52	25	15	1.1	0.7
70566-H03	515	1597	179	647	533	74	(67)	83	55	49	1.0	1.0
70566-H05	305	1250	130	374	418	30	(27)	70	29	22	0.9	0.6
70566-1	572	2199	241	857	691	104	(92)	125	40	68	0.5	0.5
70566-2	851	2583	274	1058	906	111	(97)	162	76	82	0.8	0.7
70566-3	677	2115	233	940	624	95	(84)	112	38	47	0.6	0.5
70566-6	380	1544	197	497	414	70	(61)	47	<4	43	<0.1	<0.1
70566-7	506	2035	227	820	635	119	(104)	145	97	54	1.3	1.0
Average	562	1814	202	740	600	89		105	54	47	0.9	0.7
SD (1σ)	187	339	36	183	146	32		36	38	16		
68613 (16.2 wt.% MgO)												
68613-A02	636	2038	228	837	1001	80	(66)	96	25	24	0.6	0.4
68613-A19	341	1646	188	586	728	66	(60)	84	80	24	2.2	1.4
68613-A20	510	1911	208	594	815	55	(51)	75	60	24	1.7	1.2
68613-H01	353	1744	183	525	660	65	(60)	85	24	35	0.5	0.4
68613-H02	748	1898	201	703	694	63	(60)	76	18	34	0.4	0.4
68613-H03	367	1716	181	499	651	45	(40)	80	149	19	4.7	2.8
68613-H04	832	2046	221	762	784	91	(89)	121	28	37	0.5	0.3
Average	541	1857	201	644	762	66		88	55	28	1.5	1.0
SD (1σ)	201	158	19	126	122	15		16	47	7		

(*continued on next page*)

Table A4 (*continued*)

Sample no.	V (ppm)	Mn (ppm)	Co (ppm)	Ni (ppm)	Zn (ppm)	Rh (ppb)		Ru (ppb)	Ir (ppb)	Os (ppb)	Ir/Ir*, [a]	Ir_N/Ru_N
70531 (15.4 wt.% MgO)												
70531-A01	932	2572	282	810	892	118	(106)	135	200	61	2.7	2.2
70531-A08	319	1885	213	626	592	62	(58)	60	28	23	0.9	0.7
70531-A10	691	1961	209	601	751	47	(44)	103	127	29	2.9	1.8
70531-H02	279	1735	176	360	623	30	(29)	92	60	11	2.3	1.0
Average	555	2038	220	599	715	65		98	104	31	2.2	1.4
SD (1σ)	312	368	45	185	137	38		31	76	22		
70576 (10.5 wt.% MgO)												
70576-H01	638	1534	182	642	537	70	(62)	85	8	27	0.2	0.1
70576-H02	439	1555	177	593	544	57	(50)	98	26	45	0.5	0.4
70576-H04	602	1616	182	602	586	65	(58)	58	5	27	0.2	0.1
70576-H05	338	1183	166	754	370	86	(76)	123	45	44	0.7	0.5
70576-H06	579	1622	183	588	567	67	(59)	60	6	24	0.2	0.1
70576-H07	351	1375	191	514	453	70	(60)	66	5	51	0.1	0.1
70576-H08	554	1587	171	565	484	59	(57)	52	5	24	0.2	0.1
70576-H09	576	1616	178	588	516	65	(61)	58	6	27	0.2	0.2
Average	510	1511	179	606	507	67		75	13	34	0.3	0.2
SD (1σ)	117	155	8	70	70	9		25	15	11		
Jimberlana intrusion												
BRD11												
BRD11-190-1	1058	1816	304	890	932	<2		<10	12	<4		
BRD11-190-2	1106	1712	269	945	738	<2		<10	6	<4		
BRD11-190-3	1127	1802	287	924	817	<2		<10	11	<4		
BRD11-190-4	1093	1859	288	894	875	<2		<10	7	<4		
BRD11-190-5	1089	2065	312	874	1016	<2		<10	11	<4		
BRD11-260-1	1067	1940	274	984	1311	<2		<10	8	<4		
BRD11-260-2	925	1715	244	815	1308	<2		<10	10	<4		
BRD11-260-3	1041	1826	251	893	1291	<2		<10	11	<4		
BRD11-260-4	1018	1887	267	915	1361	<2		<10	10	<4		
Average	1058	1847	277	904	1072				10			
SD (1σ)	60	110	23	47	245				2			
NDDI												
NDDI-830-1	1650	2199	332	785	1319	<2		<10	<4	<4		
NDDI-830-2	1429	1943	285	673	1236	<2		<10	<4	<4		
NDDI-830-3	1527	2047	316	741	1087	<2		<10	<4	<4		
Average	1535	2063	311	733	1214							
SD (1σ)	111	129	24	57	118							
Bushveld complex												
UG2												
UG2-3-1	2101	1931	318	1305	1070	<2		<10	<4	<4		
UG2-3-2	1772	1726	295	1338	934	<2		<10	<4	<4		
UG2-3-3	1649	1577	275	1191	903	<2		<10	<4	<4		
UG2-3-4	1413	1397	239	1070	747	<2		<10	<4	<4		
UG2-3-5	1497	1469	252	1141	772	<2		<10	<4	<4		
UG2-5-1	1402	1274	220	933	703	<2		<10	<4	<4		
UG2-5-2	1386	1297	220	898	712	<2		<10	<4	<4		
UG2-5-3	1711	1565	272	1136	845	<2		<10	<4	<4		
UG2-5-4	1279	1255	214	958	662	<2		<10	<4	<4		
UG2-5-5	1446	1380	236	1068	740	<2		<10	<4	<4		
Average	1566	1487	254	1104	809							
SD (1σ)	245	217	35	149	127							
Merensky reef												
Mrimp-1	2494	1815	284	1079	890	<2		<10	<4	<4		
Mrimp-2	2350	1693	265	993	837	<2		<10	<4	<4		
Mrimp-3	3092	2213	344	1247	1028	<2		<10	<4	<4		
Average	2645	1907	297	1106	918							
SD (1σ)	393	272	41	129	99							

Data were measured by LA-ICP-MS.

Numbers in brackets are Rh data calibrated using NIST 612. Note that these values are similar to Rh data calibrated using po727 sulfide standard.

[a] $Ir/Ir^* = Ir_N/(Ru_N \times Os_N)^{1/2}$.

probe analysis. The relative contributions of the host Cr spinel and the alloys to element concentrations in the host + inclusion mixed segment were assessed by assuming that the host Cr spinel contains no Pt and that alloy inclusions from high Mg# Cr spinels contain 90 wt.% Pt and those from low Mg# Cr spinels contain 80 wt.%. The elements contributions from the host Cr spinel were subtracted according to Cr spinel/alloy mass ratio and the results are reported in Table A1. The results are comparable to the Pt–Fe alloy composition measured by electron microprobe (Table 4). This calculation must be regarded as semi-quantitative with large analytical uncertainties. Since the Fe content of the alloy was not measured the totals of the most Pt–Fe alloys are slightly less than 100 wt.%.

REFERENCES

Ahmed A. H. and Arai S. (2002) Unexpectedly high-PGE chromitite from the deeper mantle section of the northern Oman ophiolite and its tectonic implications. *Contrib. Mineral. Petrol.* **143**, 263–278.

Ahmed A. H., Arai S., Abdel-Aziz Y. M., Ikenne M. and Rahimi A. (2009) Platinum-group elements distribution and spinel composition in podiform chromitites and associated rocks from the upper mantle section of the Neoproterozoic Bou Azzer ophiolite, Anti-Atlas, Morocco. *J. Afr. Earth Sci.* **55**, 92–104.

Anders E. and Grevesse N. (1989) Abundances of the elements – meteoritic and solar. *Geochim. Cosmochim. Acta* **53**, 197–214.

Ariskin A. A. and Nikolaev G. S. (1996) An empirical model for the calculation of spinel melt equilibria in mafic igneous systems at atmospheric pressure.1. Chromian spinels. *Contrib. Mineral. Petrol.* **123**, 282–292.

Ballhaus C. and Sylvester P. (2000) Noble metal enrichment processes in the Merensky Reef, Bushveld complex. *J. Petrol.* **41**, 545–561.

Ballhaus C., Berry R. F. and Green D. H. (1991) High-pressure experimental calibration of the olivine-ortho-pyroxene-spinel oxygen geobarometer – implications for the oxidation-state of the upper mantle. *Contrib. Mineral. Petrol.* **107**, 27–40.

Barnes S. J. (1998) Chromite in komatiites, 1. Magmatic controls on crystallization and composition. *J. Petrol.* **39**, 1689–1720.

Barnes S. J. (2000) Chromite in komatiites, II. Modification during greenschist to mid-amphibolite facies metamorphism. *J. Petrol.* **41**, 387–409.

Barnes S. J. and Brand N. W. (1999) The distribution of Cr, Ni, and chromite in komatiites, and application to exploration for komatiite-hosted nickel sulfide deposits. *Econ. Geol. Bull. Soc.* **94**, 129–132.

Barnes S. J. and Maier W. D. (2002) Platinum-group elements and microstructures of normal Merensky Reef from Impala Platinum Mines, Bushveld complex. *J. Petrol.* **43**, 103–128.

Barnes S. J. and Roeder P. L. (2001) The range of spinel compositions in terrestrial mafic and ultramafic rocks. *J. Petrol.* **42**, 2279–2302.

Barnes S. J., Prichard H. M., Cox R. A., Fisher P. C. and Godel B. (2008) The location of the chalcophile and siderophile elements in platinum-group element ore deposits (a textural, microbeam and whole rock geochemical study): implications for the fortnation of the deposits. *Chem. Geol.* **248**, 295–317.

Borisov A. and Nachtweyh K. (1998) *Ru solubility in silicate melts: experimental results in oxidizing region*. Lunar and Planetary Science XXIX, Lunar Planet. Inst., Houston.

Borisov A. and Palme H. (1995) The solubility of iridium in silicate melts – new data from experiments with Ir10pt90 alloys. *Geochim. Cosmochim. Acta* **59**, 481–485.

Borisov A. and Palme H. (1997) Experimental determination of the solubility of platinum in silicate melts. *Geochim. Cosmochim. Acta* **61**, 4349–4357.

Borisov A. and Palme H. (2000) Solubilities of noble metals in Fe-containing silicate melts as derived from experiments in Fe-free systems. *Am. Mineral.* **85**, 1665–1673.

Brenan J. M., McDonough W. F. and Dalpe C. (2003) Experimental constraints on the partitioning of rhenium and some platinum-group elements between olivine and silicate melt. *Earth Planet. Sci. Lett.* **212**, 135–150.

Brenan J. M., McDonough W. F. and Ash R. (2005) An experimental study of the solubility and partitioning of iridium, osmium and gold between olivine and silicate melt. *Earth Planet. Sci. Lett.* **237**, 855–872.

Brenan J. M., Finnigan C. F., McDonough W. F., and Homolova V. (2011) Experimental constraints on the partitioning of Ru, Rh, Ir, Pt and Pd between chromite and silicate melt: the importance of ferric iron. *Chem. Geol.*, in press, doi:10.1016/j.chemgeo.2011.05.015.

Brugmann G. E., Arndt N. T., Hofmann A. W. and Tobschall H. J. (1987) Noble-metal abundances in komatiite suites from Alexo, Ontario, and Gorgona-Island, Colombia. *Geochim. Cosmochim. Acta* **51**, 2159–2169.

Buchl A., Brugmann G. and Batanova V. G. (2004) Formation of podiform chromitite deposits: implications from PGE abundances and Os isotopic compositions of chromites from the Troodos complex, Cyprus. *Chem. Geol.* **208**, 217–232.

Burns R. G. (1970) *Mineralogical Applications of Crystal Field Theory*. Cambridge University Press, Cambridge.

Capobianco C. J. (1993) On the thermal-decomposition of Mgrh2o4 spinel and the solid–solution Mg(Rh, Al)2o4. *Thermochim. Acta* **220**, 7–16.

Capobianco C. J. and Drake M. J. (1990) Partitioning of ruthenium, rhodium, and palladium between spinel and silicate melt and implications for platinum group element fractionation trends. *Geochim. Cosmochim. Acta* **54**, 869–874.

Capobianco C. J., Hervig R. L. and Drake M. J. (1994) Experiments on crystal liquid partitioning of Ru, Rh and Pd for magnetite and hematite solid–solutions crystallized from silicate melt. *Chem. Geol.* **113**, 23–43.

Collot J. Y., Daniel J. and Burne R. V. (1985) Recent tectonics associated with the subduction collision of the Dentrecasteaux zone in the Central New-Hebrides. *Tectonophysics* **112**, 325–356.

Crocket J. H. and Macrae W. E. (1986) Platinum-group element distribution in komatiitic and tholeiitic volcanic-rocks from Munro township, Ontario. *Econ. Geol.* **81**, 1242–1251.

Dale C. W., Burton K. W., Pearson D. G., Gannoun A., Alard O., Argles T. W. and Parkinson I. J. (2009) Highly siderophile element behaviour accompanying subduction of oceanic crust: whole rock and mineral-scale insights from a high-pressure terrain. *Geochim. Cosmochim. Acta* **73**, 1394–1416.

Danyushevsky L. V. and Plechov P. (2011) Petrolog3: Integrated software for modeling crystallization processes. *Geochem. Geophy. Geosy.* **12**, 2011GC003516.

Eales H. V. and Reynolds I. M. (1986) Cryptic Variations within chromitites of the upper critical zone, northwestern Bushveld complex. *Econ. Geol.* **81**, 1056–1066.

Eggins S. M. (1993) Origin and differentiation of picritic arc magmas, Ambae (Aoba), Vanuatu. *Contrib. Mineral. Petrol.* **114**, 79–100.

Ertel W., O'Neill H. S., Sylvester P. J. and Dingwell D. B. (1999) Solubilities of Pt and Rh in a haplobasaltic silicate melt at 1300 degrees C. *Geochim. Cosmochim. Acta* **63**, 2439–2449.

Ertel W., O'Neill H. S., Sylvester P. J., Dingwell D. B. and Spettel B. (2001) The solubility of rhenium in silicate melts: implications for the geochemical properties of rhenium at high temperatures. *Geochim. Cosmochim. Acta* **65**, 2161–2170.

Finnigan C. S., Brenan J. M., Mungall J. E. and McDonough W. F. (2008) Experiments and models bearing on the role of chromite as a collector of platinum group minerals by local reduction. *J. Petrol.* **49**, 1647–1665.

Fiorentini M. L., Stone W. E., Beresford S. W. and Barley M. E. (2004) Platinum-group element alloy inclusions in chromites from Archaean mafic-ultramafic units: evidence from the Abitibi and the Agnew-Wiluna Greenstone Belts. *Mineral. Petrol.* **82**, 341–355.

Fonseca R. O. C., Campbell I. H., O'Neill H. S. C. and Allen C. M. (2009) Solubility of Pt in sulphide mattes: Implications for the genesis of PGE-rich horizons in layered intrusions. *Geochim. Cosmochim. Acta* **73**, 5764–5777.

Fortenfant S. S., Gunther D., Dingwell D. B. and Rubie D. C. (2003) Temperature dependence of Pt and Rh solubilities in a haplobasaltic melt. *Geochim. Cosmochim. Acta* **67**, 123–131.

Fortenfant S. S., Dingwell D. B., Ertel-Ingrisch W., Capmas F., Birck J. L. and Dalpe C. (2006) Oxygen fugacity dependence of Os solubility in haplobasaltic melt. *Geochim. Cosmochim. Acta* **70**, 742–756.

Gao S., Liu X. M., Yuan H. L., Hattendorf B., Gunther D., Chen L. and Hu S. H. (2002) Determination of forty two major and trace elements in USGS and NIST SRM glasses by laser ablation-inductively coupled plasma-mass spectrometry. *Geostand Newslett. – J. Geostand Geoanal.* **26**, 181–196.

Geschwind S. and Remeika J. P. (1962) Spin resonance of transition metal ions in corundum. *J. Appl. Phys.* **33**, 370.

Gijbels R. H., Millard H. T., Desborough G. A. and Bartel A. J. (1974) Osmium, ruthenium, iridium and uranium in silicates and chromite from eastern Bushveld complex, South-Africa. *Geochim.Cosmochim. Acta* **38**, 319–337.

Gorton M. P. (1977) Geochemistry and origin of quaternary volcanism in New-Hebrides. *Geochim. Cosmochim. Acta* **41**, 1257–1270.

Halter W. E., Pettke T., Heinrich C. A. and Rothen-Rutishauser B. (2002) Major to trace element analysis of melt inclusions by laser-ablation ICP-MS: methods of quantification. *Chem. Geol.* **183**, 63–86.

Hamlyn P. R., Keays R. R., Cameron W. E., Crawford A. J. and Waldron H. M. (1985) Precious metals in magnesian low-Ti lavas – implications for metallogenesis and sulfur saturation in primary magmas. *Geochim. Cosmochim. Acta* **49**, 1797–1811.

Horn I., Foley S. F., Jackson S. E. and Jenner G. A. (1994) Experimentally determined partitioning of high-field strength-elements and selected transition-elements between spinel and basaltic melt. *Chem. Geol.* **117**, 193–218.

Ireland T. J., Walker R. J. and Garcia M. O. (2009) Highly siderophile element and Os-187 isotope systematics of Hawaiian picrites: implications for parental melt composition and source heterogeneity. *Chem. Geol.* **260**, 112–128.

Irvine T. N. (1967) Chromian spinel as a petrogenetic indicator. Part. 2 Petrologic implications. *Can. J. Earth Sci.* **4**, 71–103.

Kamenetsky V. S., Crawford A. J. and Meffre S. (2001) Factors controlling chemistry of magmatic spinel: an empirical study of associated olivine, Cr-spinel and melt inclusions from primitive rocks. *J. Petrol.* **42**, 655–671.

Keays R. R. and Campbell I. H. (1981) Precious metals in the Jimberlana intrusion, western-Australia – implications for the genesis of platiniferous ores in layered intrusions. *Econ. Geol.* **76**, 1118–1141.

Kilinc A., Carmichael I. S. E., Rivers M. L. and Sack R. O. (1983) The ferric–ferrous ratio of natural silicate liquids equilibrated in air. *Contrib. Mineral. Petrol.* **83**, 136–140.

Locmelis M., Pearson N. J., Barnes S. J. and Fiorentini M. L. (2011) Ruthenium in komatiitic chromite. *Geochim. Cosmochim. Acta* **75**, 3645–3661.

Longerich H. P., Jackson S. E. and Gunther D. (1996) Laser ablation inductively coupled plasma mass spectrometric transient signal data acquisition and analyte concentration calculation. *J. Anal. At. Spectrom.* **11**, 899–904.

Maier W. D., Barnes S. J., DeKlerk W. J., Teigler B. and Mitchell A. A. (1996) Cu/Pd and Cu/Pt of silicate rocks in the Bushveld complex: implications for platinum-group element exploration. *Econ. Geol. Bull. Soc.* **91**, 1151–1158.

Meisel T., Fellner N. and Moser J. (2003) A simple procedure for the determination of platinum group elements and rhenium (Ru, Rh, Pd, Re, Os Ir and Pt) using ID-ICP-MS with an inexpensive on-line matrix separation in geological and environmental materials (vol. 18, p. 720, 2003). *J. Anal. At. Spectrom.* **18**, 1318.

Meisel T. and Moser J. (2004) Platinum-group element and rhenium concentrations in low abundance reference materials. *Geostand. Geoanal. Res.* **28**, 233–250.

Mondal S. K. and Mathez E. A. (2007) Origin of the UG2 chromitite layer, Bushveld complex. *J. Petrol.* **48**, 495–510.

Murck B. W. and Campbell I. H. (1986) The effects of temperature, oxygen fugacity and melt composition on the behavior of chromium in basic and ultrabasic melts. *Geochim. Cosmochim. Acta* **50**, 1871–1887.

Naldrett A. J., Kinnaird J., Wilson A., Yudovskaya M., MacQuade S., Chunnett G. and Stanley C. (2009) Chromite composition and PGE content of Bushveld chromitites: Part 1 – the lower and middle groups. *Appl. Earth Sci.* **118**, 131–161.

Nell J. and O'Neill H. S. C. (1997) The Gibbs free energy of formation and heat capacity of beta-Rh2O3 and MgRh2O4, the MgO–Rh–O phase diagram, and constraints on the stability of Mg2Rh4+O4. *Geochim. Cosmochim. Acta* **61**, 4159–4171.

Pagé P. and Barnes S. J. (2009) Using Trace Elements in Chromites to Constrain the Origin of Podiform Chromitites in the Thetford Mines Ophiolite, Quebec, Canada. *Econ. Geol.* **104**, 997–1018.

Pagé P., Barnes S. J., Bédard J. H., and Zientek M. L. (2011) In situ determination of Os, Ir, and Ru in chromites formed from komatiite, tholeiite and boninite magmas: implications for chromite control of Os, Ir and Ru during partial melting and crystal fractionation. *Chem. Geol.*, in press, doi:10.1016/j.chemgeo.2011.06.006.

Peck D. C., Keays R. R. and Ford R. J. (1992) Direct crystallization of refractory platinum-group element alloys from boninitic magmas – evidence from western Tasmania. *Aust. J. Earth Sci.* **39**, 373–387.

Peucker-Ehrenbrink B., Bach W., Hart S. R., Blusztajn J. S. and Abbruzzese T. (2003) Rhenium–osmium isotope systematics and platinum group element concentrations in oceanic crust from DSDP/ODP sites 504 and 417/418. *Geochem. Geophys. Geosyst.* **4**, 2002GC000414.

Pitcher L., Helz R. T., Walker R. J. and Piccoli P. (2009) Fractionation of the platinum-group elements and Re during crystallization of basalt in Kilauea Iki Lava Lake, Hawaii. *Chem. Geol.* **260**, 196–210.

Puchtel I. S. and Humayun M. (2001) Platinum group element fractionation in a komatiitic basalt lava lake. *Geochim. Cosmochim. Acta* **65**, 2979–2993.

Ramsay W. R. H., Crawford A. J. and Foden J. D. (1984) Field setting, mineralogy, chemistry, and genesis of arc picrites, New-Georgia, Solomon-Islands. *Contrib. Mineral. Petrol.* **88**, 386–402.

Ravizza G. and Pyle D. (1997) PGE and Os isotopic analyses of single sample aliquots with NiS fire assay preconcentration. *Chem. Geol.* **141**, 251–268.

Righter K. and Downs R. T. (2001) The crystal structures of synthetic Re- and PGE-bearing magnesioferrite spinels: implications for impacts, accretion and the mantle. *Geophys. Res. Lett.* **28**, 619–622.

Righter K., Campbell A. J., Humayun M. and Hervig R. L. (2004) Partitioning of Ru, Rh, Pd, Re, Ir, and Au between Cr-bearing spinel, olivine, pyroxene and silicate melts. *Geochim. Cosmochim. Acta* **68**, 867–880.

Roeder P. L. and Campbell I. H. (1985) The effect of postcumulus reactions on composition of chrome-spinels from the Jimberlana intrusion. *J. Petrol.* **26**, 763–786.

Roeder P. L. and Emslie R. F. (1970) Olivine-liquid equilibrium. *Contrib. Mineral. Petrol.* **29**, 275.

Sattari P., Brenan J. M., Horn I. and McDonough W. F. (2002) Experimental constraints on the sulfide- and chromite-silicate melt partitioning behavior of rhenium and platinum-group elements. *Econ. Geol. Bull. Soc.* **97**, 385–398.

Scowen P. A. H., Roeder P. L. and Helz R. T. (1991) Reequilibration of chromite within Kilauea Iki Lava Lake, Hawaii. *Contrib. Mineral. Petrol.* **107**, 8–20.

Setiabudi B. T., Campbell I. H., Martin C. E. and Allen C. M. (2007) Platinum group element geochemistry of andesite intrusions of the Kelian region, East Kalimantan, Indonesia: implications of gold depletion in the intrusions associated with the Kelian gold deposit. *Econ. Geol.* **102**, 95–108.

Shannon R. D. (1976) Revised effective ionic-radii and systematic studies of interatomic distances in halides and chalcogenides. *Acta Crystallogr., Sect. A: Found.* **32**, 751–767.

Sylvester P. J. and Eggins S. M. (1997) Analysis of Re, Au, Pd, Pt and Rh in NIST glass certified reference materials and natural basalt glasses by laser ablation ICP-MS. *Geostand. Newslett. – J. Geostand. Geoanal.* **21**, 215–229.

Tredoux M., Lindsay N. M., Davies G. and McDonald I. (1995) The fractionation of platinum-group elements in magmatic systems, with the suggestion of a novel causal mechanism. *S. Afr. J. Geol.* **98**, 157–167.

Warden A. J. (1970) Evolution of Aoba caldera volcano, New Hebrides. *Bull. Volcanol.* **34**, 107–140.

Woodland S. J., Pearson D. G. and Thirlwall M. F. (2002) A platinum group element and Re–Os isotope investigation of siderophile element recycling in subduction zones: comparison of Grenada, Lesser Antilles arc, and the Izu-Bonin arc. *J. Petrol.* **43**, 171–198.

Zhang S. X., Wu S. Y., Xu P. and Li L. L. (2010) Theoretical investigations on the spin Hamiltonian parameters and the local structure for Rh(2+) in rutile. *Can. J. Phys.* **88**, 49–53.

Zhou M. F., Sun M., Keays R. R. and Kerrich R. W. (1998) Controls on platinum-group elemental distributions of podiform chromitites: a case study of high-Cr and high-Al chromitites from Chinese orogenic belts. *Geochim. Cosmochim. Acta* **62**, 677–688.

Zoller W. H., Parrington J. R. and Kotra J. M. P. (1983) Iridium enrichment in airborne particles from Kilauea volcano – january 1983. *Science* **222**, 1118–1121.

Associate editor: Mark Rehkamper